

Microstructural imaging of human neocortex in vivo

Luke J. Edwards^{a,*}, Evgeniya Kirilina^{a,b}, Siawoosh Mohammadi^{a,c}, Nikolaus Weiskopf^a

^a Department of Neurophysics, Max Planck Institute for Human Cognitive and Brain Sciences, Leipzig, Germany

^b Neurocomputation and Neuroimaging Unit, Center for Cognitive Neuroscience Berlin, Freie Universität Berlin, Germany

^c Institute of Systems Neuroscience, University Medical Center Hamburg-Eppendorf, Hamburg, Germany

ARTICLE INFO

Keywords:

hMRI
Quantitative
High resolution
Gray matter

ABSTRACT

The neocortex of the human brain is the seat of higher brain function. Modern imaging techniques, chief among them magnetic resonance imaging (MRI), allow non-invasive imaging of this important structure.

Knowledge of the microstructure of the neocortex has classically come from post-mortem histological studies of human tissue, and extrapolations from invasive animal studies. From these studies, we know that the scale of important neocortical structure spans six orders of magnitude, ranging from the size of axonal diameters (microns), to the size of cortical areas responsible for integrating sensory information (centimetres). MRI presents an opportunity to move beyond classical methods, because MRI is non-invasive and MRI contrast is sensitive to neocortical microstructure over all these length scales. MRI thus allows inferences to be made about neocortical microstructure in vivo, i.e. MRI-based in vivo histology.

We review recent literature that has applied and developed MRI-based in vivo histology to probe the microstructure of the human neocortex, focusing specifically on myelin, iron, and neuronal fibre mapping. We find that applications such as cortical parcellation (using R_1 maps as proxies for myelin content) and investigation of cortical iron deposition with age (using R_2^* maps) are already contributing to the frontiers of knowledge in neuroscience. Neuronal fibre mapping in the cortex remains challenging in vivo, but recent improvements in diffusion MRI hold promise for exciting applications in the near future. The literature also suggests that utilising multiple complementary quantitative MRI maps could increase the specificity of inferences about neocortical microstructure relative to contemporary techniques, but that further investment in modelling is required to appropriately combine the maps.

In vivo histology of human neocortical microstructure is undergoing rapid development. Future developments will improve its specificity, sensitivity, and clinical applicability, granting an ever greater ability to investigate neuroscientific and clinical questions about the human neocortex.

Introduction: structure, function, and beyond

Modern imaging methods allow a unique, non-invasive glimpse into the organisation of the living human brain. Magnetic resonance imaging

(MRI) in particular has the potential to answer questions about structure–function relationships, thanks to its unique ability to measure both structure and function in the same brain longitudinally over a wide range of spatial scales (Turner and De Haan, 2017; Draganski and May, 2008;

Abbreviations: ALS, amyotrophic lateral sclerosis; AP, absolute pitch; B_0 , magnetic field induction; BOLD, blood oxygenation level-dependent; CEST, chemical exchange saturation transfer; CNR, contrast-to-noise ratio; COx, cytochrome c oxidase; CSF, cerebrospinal fluid; dMRI, diffusion MRI; DTI, diffusion tensor imaging; [Fe], iron concentration; fMRI, functional MRI; FWE-DTI, free water elimination-DTI; HARDI, high angular resolution diffusion imaging; hMRI, in vivo histology using MRI; HR, high resolution; M1, primary motor cortex; MEG, magnetoencephalography; mOFC, medial orbitofrontal cortex; MR, magnetic resonance; MRE, MR elastography; MRI, MR imaging; MRS, MR spectroscopy; MSMT-CSD, multishell multitissue-constrained spherical deconvolution; MT, magnetization transfer; MTR, MT ratio; MTsat, MT saturation; NODDI, neurite orientation dispersion and density imaging; OD, orientation dispersion; PD, proton density; PDw, PD-weighted; qMRI, quantitative MRI; QSM, quantitative susceptibility mapping; R_1 , longitudinal relaxation rate; R_2 , transverse relaxation rate; R_2^* , effective transverse relaxation rate; RF, radiofrequency; S1, primary somatosensory cortex; SNR, signal-to-noise ratio; T_1 , longitudinal relaxation time; T_1w , T_1 -weighted; T_2 , transverse relaxation time; T_2w , T_2 -weighted; T_2^* , effective transverse relaxation time; T_2^*w , T_2^* -weighted; TIs, inversion times; V1, primary visual cortex; V2, secondary visual cortex; V3, tertiary visual cortex; V5/MT, quinary visual cortex/middle temporal visual area.

* Corresponding author.

E-mail address: ledwards@cbs.mpg.de (L.J. Edwards).

<https://doi.org/10.1016/j.neuroimage.2018.02.055>

Received 9 October 2017; Received in revised form 13 February 2018; Accepted 26 February 2018

Available online 26 March 2018

1053-8119/© 2018 The Authors. Published by Elsevier Inc. This is an open access article under the CC BY license (<http://creativecommons.org/licenses/by/4.0/>).

Van Essen et al., 2012).

In vivo MRI techniques for analysing macroscopic (0.5 mm–200 mm) brain features (e.g. cortical thickness (Fischl and Dale, 2000), gyrification (Luders et al., 2006), and the boundaries and extent of some functional areas (Serenio et al., 1995; Wernking et al., 2002)) are now routine in neuroscientific and clinical studies (Symms et al., 2004; Bridge and Clare, 2006; Van Essen et al., 2012). Important insights into the structure–function relationship have been gained through the use of these techniques to relate macroscopic brain anatomy to functional brain organisation (Fischl and Dale, 2000; Mechelli et al., 2005; Draganski and May, 2008).

Recent progress in high field MRI (Lerch et al., 2017; Trampel et al., 2018; Turner and De Haan, 2017) has pushed accessible image-resolutions into the “mesoscopic scale”, enabling in-vivo imaging of features including cortical myeloarchitectonic laminæ (Trampel et al., 2018), functionally-defined cortical columns (Yacoub et al., 2008; Nasr et al., 2016; Dumoulin et al., 2018), dural lymphatic vessels (Absinta et al., 2017), and vasculature (Koopmans et al., 2008). There is not yet consensus in the MRI community as to the precise definition of the mesoscopic scale (contrast the conflicting definitions in Novikov et al., 2016; Lerch et al., 2017; Dumoulin et al., 2018); for concreteness in the following, we set the boundaries at 0.1 mm–0.5 mm.

Unfortunately, microscopic structures (< 0.1 mm) such as neurons (Zilles et al., 2002) and glial cells (Barres et al., 2015) cannot be directly resolved with in vivo MRI in humans. Direct imaging of such small structures requires invasive ex vivo histology, or very time-consuming ex vivo MRI microscopy scans (Bulte et al., 2002).

However, some information about the microstructure is retained at the resolutions possible with in vivo MRI: the combination of biophysical models of magnetic resonance (MR) contrast with advances in quantitative MRI allows one to make indirect inferences about the microscopic structures of the brain in vivo with whole brain coverage, i.e. MRI can enable in vivo histology (Bridge and Clare, 2006; Deistung et al., 2013; Weiskopf et al., 2015; Lerch et al., 2017). Following Weiskopf et al. (2015), we abbreviate “in vivo histology using MRI” as hMRI.

Access to microstructural information in vivo, as promised by hMRI, has the potential to revolutionise clinical and fundamental neuroscience (Zatorre et al., 2012; Turner and De Haan, 2017), as it would permit longitudinal studies of microstructure in conjunction with functional imaging, training studies, and investigations into pathology.

This review gives an overview of the rapidly developing field of neocortical hMRI, examining recent literature pushing the frontiers of resolution and specificity. Though we focus primarily on in vivo imaging of structural features, aspects of in vivo functional MRI (fMRI) are also included where needed. Sub-cortical nuclei and the white matter of the brain are beyond the scope of this review, though this omission should neither be taken to imply a lack of importance of these structures for brain function (Zatorre et al., 2012; Forstmann et al., 2016), nor a lack of MRI studies investigating them (Deistung et al., 2013; Stikov and Pike, *this special issue*).

We begin with a short overview of the functional and structural organisation of human neocortex at the macro-, meso-, and microstructural scales (Fig. 1). We then describe how these anatomical and functional features drive structural MRI contrast, and review contemporary literature on cortical microstructural mapping using MRI. The literature review has three main foci: mapping of intracortical myelin, mapping of intracortical neuronal fibres, and mapping of intracortical iron. In the final section we sketch our view of the possible future of this exciting new emerging research area.

Cortical architecture: what we want to see!

The accepted picture of human neocortex arising from the cytoarchitectonic work of early pioneers such as Brodmann (1909) is that the human neocortex is subdivided by changes in neuron-morphology and -spatial distribution into six mesoscopic laminæ, conventionally labelled

with the roman numerals I–VI (Fig. 1d). Although the whole neocortex has this six-layer organisation, the neuronal cell body density and size distribution within the laminæ are only constant over limited macroscopic regions of the cortex, giving rise to distinct cytoarchitectonic areas (Brodmann, 1909; von Economo and Koskinas, 1925). The neocortex can be parcellated on the basis of these cytoarchitectonically consistent areas; an example is shown in Fig. 1a. Modern histological techniques and automated image analysis methods have improved upon the quality and granularity of such cytoarchitectonic parcellations (Zilles and Amunts, 2010; Amunts and Zilles, 2015; Ding et al., 2016).

The correspondence of individual cytoarchitectonic areas to specific functions has been validated for many sensory and motor functional areas of the cortex (including through investigation of the laminar and areal dependent distribution of neurotransmitter binding sites (Zilles et al., 2002, 2015; Palomero-Gallagher and Zilles, 2017)). It has further been found that cytoarchitectonically similar areas are more likely to be functionally connected (Hilgetag and Amunts, 2016; Beul et al., 2017).

Studies of microscopic myeloarchitecture carried out in parallel to classical cytoarchitectonic investigations found a similar six-layer pattern of myelin density (Fig. 1d), which was used to define myeloarchitectonic cortical parcellations (an example is shown in Fig. 1b). However, a complete histological myeloarchitectonic parcellation of human cortex is, at time of writing, still lacking (Vogt and Vogt, 1919; Annesse et al., 2004; Nieuwenhuys et al., 2015b; Nieuwenhuys and Broere, 2017). Myeloarchitectonic parcellations appear to share some areal borders with cytoarchitectonic parcellations (Vogt and Vogt, 1919), although disagreements over the number and extent of cyto- and myeloarchitectonic areas mean that a one-to-one correspondence has not been confirmed (Braak, 1980; Amunts and Zilles, 2015; Glasser et al., 2016).

A hypothesis explaining both the similar six-layer structure and the similar parcellations asserts that the bands of Baillarger (Fig. 1d), the most striking feature of cortical myelination patterns, are dominated by axonal-collaterals (axonal branches extending parallel to the cortical surface) of pyramidal neuron-axons descending towards the white matter, and that the density of myelin is thus related to the size and density of pyramidal neurons in the layers above (Braitenberg, 1962; Hellwig, 1993; Dinse et al., 2015). While this model is an oversimplification (most notably in its omission of afferent axons and their collaterals), Hellwig (1993) showed that applying the model to tabulated cytoarchitectonic data of several cytoarchitectonic areas resulted in predicted bands of Baillarger that were recognisably similar to those visible in histological myelin stains from the corresponding myeloarchitectonic area.

The myelin ensheathing axons is a complex structure composed of highly ordered lipids (~70% dry mass), proteins (~30% dry mass) and trapped water (~40% water content; Morell et al., 1994). It is worth bearing in mind that these biochemical components are not all unique to myelin, and many, especially lipids, may be found in other biological compartments (Morell et al., 1994). Myelin properties differ in cortex relative to measurements in white matter tracts (Morell et al., 1994), and it has been suggested that myelin properties may also be cortical-layer dependent (Micheva et al., 2016).

Histological sections of cortex stained for myelin show fibres predominantly oriented either perpendicular or parallel to the cortical surface (radial and tangential fibres, respectively; Fig. 1d). Radial myelinated fibres comprise afferent fibres entering the cortex from other cortical areas and sub-cortical nuclei, efferent fibres from pyramidal neurons leaving the cortex, and some intracortical short axons. The density of radially orientated myelinated fibres thus largely reflects the density of cortico-cortical and cortico-nuclear connections leaving/entering the cortex. Tangential myelinated fibres are axonal collaterals and, in some laminæ, tangentially running axons, thus their density reflects the degree of local cortical connectivity. Little is known about the pattern of preferential orientation of tangential fibres in the plane parallel to the cortical sheet in human cortex (Rockland, 2017). Such information is difficult to gather with the classical 2d histology techniques that are possible in post mortem human tissue (Rockland, 2017). The

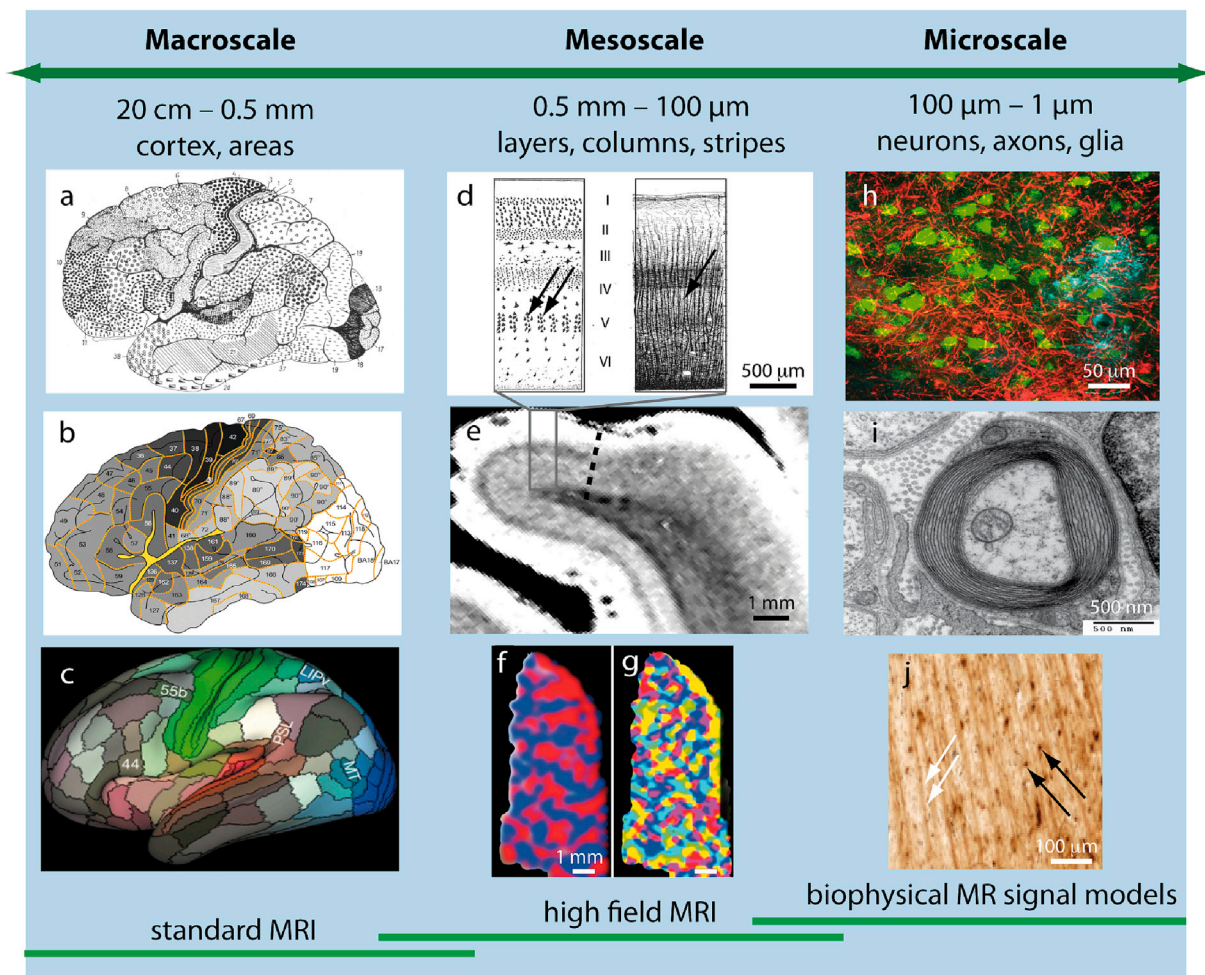


Fig. 1. Examples of neocortical organisation on the macroscopic (a–c), mesoscopic (d–g), and microscopic (h–j) scales. On the macroscopic scale, the cortex can be parcellated into areas on the basis of cytoarchitecture, myeloarchitecture, and functional specialisation. (a) The classic cytoarchitectonic parcellation from [Brodmann \(1909\)](#). (b) A myeloarchitectonic parcellation compiled by [Nieuwenhuys and Broere \(2017\)](#) from classic myeloarchitectonic works; this parcellation is incomplete in the occipital lobe. Higher myelin density is shown by darker shading; high myelin density is present in primary motor and sensory areas. The parcellation is similar to cytoarchitectonic parcellations. (c) A recent *in vivo* cortical parcellation based on combining structural and functional MRI, which revealed subdivisions very similar to classic cyto- and myeloarchitectonic parcellations. Reprinted by permission from the Nature Publishing Group: Nature ([Glasser et al., 2016](#)), copyright (2016). On the mesoscopic scale, the cortex can be subdivided into six distinct layers based on cytoarchitecture (d, left) or myeloarchitecture (d, right); figure adapted from [Vogt and Vogt \(1919\)](#). Bands of Baillarger are visible as horizontal stripes of increased myelin density in layers IV and V of (d, right). Mesoscopic ontogenetic columns (columns of increased neuron cell body density and decreased myelin density) are indicated by arrows in (d). (e) High resolution T_2^+ -weighted MR image showing that distinct cortical layers, as well as the border between primary and secondary visual cortices (dotted line), are distinguishable using MRI (post mortem human brain sample acquired at 7 T). Contrast between the layers arises due to differing myelin density and iron concentration. Functional units are also found on the mesoscopic scale, with functional cortical columns representing cortical processing units. Examples of these functional cortical columns are (f) ocular dominance and (g) orientational preference columns in human visual cortex (reprinted from [Yacoub et al. \(2008\)](#), copyright (2008) National Academy of Sciences). On the microscopic scale, neuronal cell bodies, myelinated fibres, and glial cells are important constituents of the cortex. (h) Fluorescent microscopy image of a sample of human cortex from the temporal lobe (adapted from [Morawski et al. \(2018\)](#)) showing neuronal cell bodies (HuC/D marker, green), myelinated fibres (myelin basic protein stain, red) and astroglia (GFAP stain, cyan). (i) The myelin sheath around axonal fibres can be imaged using electron microscopy; shown here is an electron micrograph of a human post mortem sample from the superior longitudinal fasciculus, reproduced from [Liewald et al. \(2014\)](#). (j) Iron localised in oligodendrocytes and myelinated fibres is an important microscopic feature of the cortex which contributes to MRI contrast. Here, a Perls' stain for iron shows increased iron concentration in myelinated fibres (white arrows) and in the cell bodies of oligodendrocytes (black arrows).

problems of 2d histology for tracing connectomics are gradually being overcome with the arrival of modern 3d histological and imaging techniques ([Chung and Deisseroth, 2013](#); [Leuze et al., 2014](#); [Aggarwal et al., 2015](#); [Hare et al., 2015](#); [Ye et al., 2016](#); [Morawski et al., 2018](#)).

Myeloarchitecture thus provides valuable information about the local connectomics of the cortex at the mesoscopic scale, i.e. the degree of cortical myelination reflects intracortical connectivity density ([Amunts and Zilles, 2015](#); [Micheva et al., 2016](#)). Moreover, changes in local cortical myelination reflecting brain maturation and plasticity could be much stronger than changes in cytoarchitecture ([Fields, 2015](#)). However, cortical myelination provides only a limited picture of the types and

density of connections between cortical neurons. Indeed, it has been argued that an important role of cortical myelin is to hinder the formation of synapses ([Braitenberg, 1962](#); [Tomassy et al., 2014](#)), implying that the heavily myelinated primary cortical areas of the neocortex could be more hardwired and less plastic than other cortical areas ([Glasser et al., 2014](#)). This purported role is in contrast to the main role of myelin in white matter, which is to accelerate the electrical signal-conduction velocity ([Fields, 2015](#)).

In addition to myelinated axons and their collaterals, the cortex also includes unmyelinated axons and neuronal dendrites ([Nieuwenhuys et al., 2008](#)). These elements contribute to the connectivity and

complexity of the structure of the cortex, and knowledge of their distribution complements the information that can be gained from myelin maps (Hayes and Lewis, 1996; Hellwig, 2002). It is pertinent to note that in cortex the number of axons and dendrites are approximately equal (Braitenberg and Schüz, 1998c; a), and that dendritic structures change with age and can vary between cortical areas (Jacobs and Scheibel, 2002).

Functional studies using invasive electrophysiological and optical recordings in animals have found mesoscopic functional subdivisions of cytoarchitectonic areas. Primate primary visual cortex provides an archetypal example: nested radial columnar structures represent the ocular dominance, orientation selectivity, movement sensitivity, colour sensitivity, and position sensitivity of a small patch of cortex (Zeki, 1993; Nieuwenhuys et al., 2008; Yacoub et al., 2008). Examples of these structures are shown in Fig. 1f and g, though these functionally defined radial columns should not be confused with the microscopic ontogenetic columnar structures visible in Fig. 1d and j, for which no functional specialisation has so far been experimentally confirmed (Rakic, 1988; Horton and Adams, 2005). Similarly, investigations of neocortical cytochrome c oxidase (COx) content, a proxy for oxidative metabolic activity (Horton, 1984), have found mesoscopic and macroscopic layer-dependent stripe- and patch-patterns of high COx content within the human visual cortex, probably related to selective thalamic input into these structures (Horton and Adams, 2005). Whether functionally specific columnar organisation is a feature throughout the entire cortex, or only a feature of specific areas, is still under debate (Horton and Adams, 2005).

Glial cells, including astroglia (Fig. 1h), microglia, oligodendrocytes (Fig. 1j) and oligodendrocyte progenitor cells, are important microstructural constituents of the neocortex that support neurons in their function (Kettenmann and Verkhratsky, 2011; Barres et al., 2015; Khakh and Sofroniew, 2015). Investigations of the distribution of glial cells across cortical depth has revealed a layer-dependency reflecting the mesoscopic cytoarchitectonic laminæ (Connor et al., 1990; Connor and Menzies, 1996; Oberheim et al., 2006), though, to the best of our knowledge, no systematic difference in glial cell density between cytoarchitectonic areas has yet been reported. Furthermore, some glial cell populations are dynamic, travelling across the brain (De Biase et al., 2017; McCarthy, 2017). This is exemplified by oligodendrocytes, whose distribution across the brain is dynamic because oligodendrocyte progenitor cells travel to active myelination hot spots (Todorich et al., 2009).

The cortical vasculature is an essential component of neocortical structure. It can be categorised into macroscopic vessels mostly situated on the pial surface, mesoscopic diving arteries and veins penetrating into the cortex, and a dense network of capillaries present throughout cortex (Duvernoy et al., 1981; Schmid et al., 2017). Vascular density varies

throughout the cortex. As examples, vascular density varies with cortical depth, with central layers having the highest vascular density (Duvernoy et al., 1981; Schmid et al., 2017); and is systematically elevated in primary cortical areas as compared to higher cortical areas (Fonta and Imbert, 2002; Schmid et al., 2017). It has also been suggested that vascular density is elevated relative to the surrounding tissue in mesoscopic COx patches in primary visual cortex (Keller et al., 2011; Hirsch et al., 2012), though this remains controversial (Adams et al., 2015).

Finally, the iron content of the neocortex is important because cortical iron load is a risk factor for several neurodegenerative diseases (Bartzokis et al., 2004; van Duijn et al., 2017).

Neocortical iron is distributed inhomogeneously in a number of different biochemical forms. Approximately 80% of neocortical iron is stored in the soluble paramagnetic iron-storage protein ferritin (Connor et al., 1990; Haacke et al., 2005; Todorich et al., 2009), which is distributed inhomogeneously among neocortical cells and sub-cellular compartments (Connor et al., 1990). The iron-transport protein transferrin, iron clusters in mitochondria, and haemoglobin (which is paramagnetic when deoxygenated) constitute the remaining iron compounds in neocortex (Zecca et al., 2004; Haacke et al., 2005).

The microscopic somata of oligodendroglia, astroglia, and microglia have high iron content (Connor et al., 1990; Connor and Menzies, 1996; Todorich et al., 2009) as compared to the somata of neocortical neurons (Morris et al., 1992; Connor and Menzies, 1996). Further, the iron load of these compartments can be dynamic. This is exemplified by microglia, whose iron-load in motor cortex has been demonstrated to become layer-dependent in the case of amyotrophic lateral sclerosis (ALS) pathology (Kwan et al., 2012). It is further known from post-mortem histological investigations that the ageing brain accumulates iron at different rates in different macroscopic cortical areas (Hallgren and Sourander, 1958).

Interestingly, myelinated fibres have been shown using ex vivo histology to have an increased iron concentration relative to the surrounding tissue in several primary cortical areas (primary visual, motor, and somatosensory cortex; Stüber et al., 2014) and in the superior parietal lobe (Fukunaga et al., 2010; Stüber et al., 2014). An example is shown in Fig. 2, where the distribution of iron and myelin have similar mesoscopic laminar structure. This may be related to iron's role as an enzymatic cofactor for the biosynthesis of cholesterol and other lipids, essential components of the myelin sheath (Morris et al., 1992; Connor and Menzies, 1996). However, there are results showing that this mesoscopic-scale relationship does not seem to extend to primary auditory cortex (Wallace et al., 2016).

Iron is usually considered a component of tissue composition, rather than part of the cortical microstructure. However, as shown above, cortical iron is inhomogeneously distributed on the microscopic,

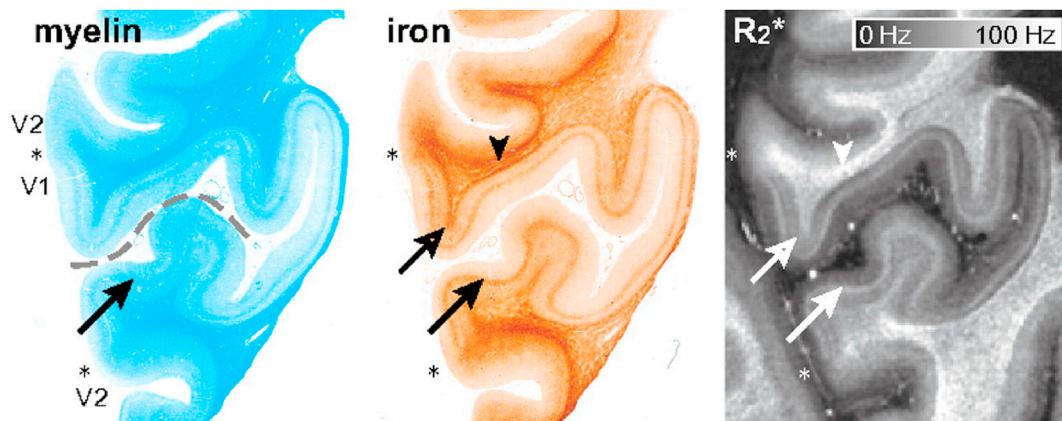


Fig. 2. Myelin and iron stains of post mortem brain tissue containing primary and secondary visual cortex, demonstrating that iron and myelin are colocalised in cortex on the mesoscopic scale in this cortical region. The dashed line shows the calcarine sulcus, and the asterisk denotes the border between primary (V1) and secondary (V2) visual cortex. Iron and myelin give rise to MRI contrast differences, as can be seen in the map of the effective transverse relaxation rate (R_2^*) on the right; specific histological features that are reproduced in this map are marked by arrows. Figure reproduced from Fukunaga et al. (2010).

mesoscopic and macroscopic scales. Probing the inhomogeneous iron distribution in vivo therefore has the potential to provide useful and specific biomarkers for compartments such as glial cells and iron rich fibres, with potential clinical impact. We thus regard cortical iron content to be a microstructural feature of cortex for the purposes of this review.

From biology to MR images: what can we really see?

The previous section illustrated the rich quantity of anatomical and functional information that could potentially be gleaned from MRI of the neocortex. However, the voxel sizes currently possible for in vivo MRI are firmly within the mesoscopic scale (see e.g. Lüsebrink et al. (2017)), and thus preclude direct imaging of microscopic cortical features. The fundamental concept underlying hMRI is that the water molecules generating the MR signal are, individually, sensitive probes of local microstructure, and that the formal averaging process that maps the signals from these individually sensitive probes to the MRI signal of a voxel does not lose all of this microstructural information (Novikov et al., 2016). This means that, although we cannot directly image microstructure using MRI in vivo, we can make some inferences about the microstructure within a voxel (Weiskopf et al., 2015).

The rest of this section is organised as follows. Sections [Quantitative MRI and its relationship to hMRI](#) and [Challenges of cortical MRI](#) introduce general considerations for cortical hMRI. Section [Quantitative MRI and its relationship to hMRI](#) introduces the concept of quantitative MRI methods, while Section [Challenges of cortical MRI](#) discusses the challenges of imaging the human cortex in vivo. Building upon these discussions, Sections [Myelin mapping: myeloarchitecture in vivo – Iron mapping: from glial cells to senile plaques](#)

mapping: from glial cells to senile plaques then view MRI contrast through the lens of biology. We examine the sensitivity of MRI methods to three important neocortical biological substrates: lipids contained within the myelin sheath (Leuze et al., 2017); paramagnetic iron encapsulated in glial cells and myelinated fibres (Stüber et al., 2014); and the neuronal fibre distribution (Leuze et al., 2014). Each of these substrates causes changes to the local environment of the water protons imaged with MRI, and thus causes changes in MRI contrast. We treat each of these biological substrates in turn, discussing the qMRI techniques that have been used to investigate them, followed by a review of neuroscientific and clinical applications. In Section [Other biological substrates and MR methods](#), we then describe other promising biological substrates that could potentially be future targets of hMRI, along with several other promising MR methods.

Fig. 3 contains a diagrammatic summary of the MRI methods that have been used to probe these three biological substrates in the reviewed articles. It must be borne in mind in the following that these three substrates are not the only biological contributors to the MRI signal; recent electron microscopic investigations demonstrate just how complex the cortex really is (Kasthuri et al., 2015). These three substrates instead represent those for which there are at present, in our view, the most well developed and well-investigated hMRI techniques.

For brevity, we have reviewed only articles containing studies on human subjects and/or tissues in Sections [Myelin mapping: myeloarchitecture in vivo – Iron mapping: from glial cells to senile plaques](#). Ex vivo studies have only been included when no suitable in vivo study could be found. Articles which treat cortex as homogeneous (i.e. they do not examine laminar structure or differences between cortical areas) have

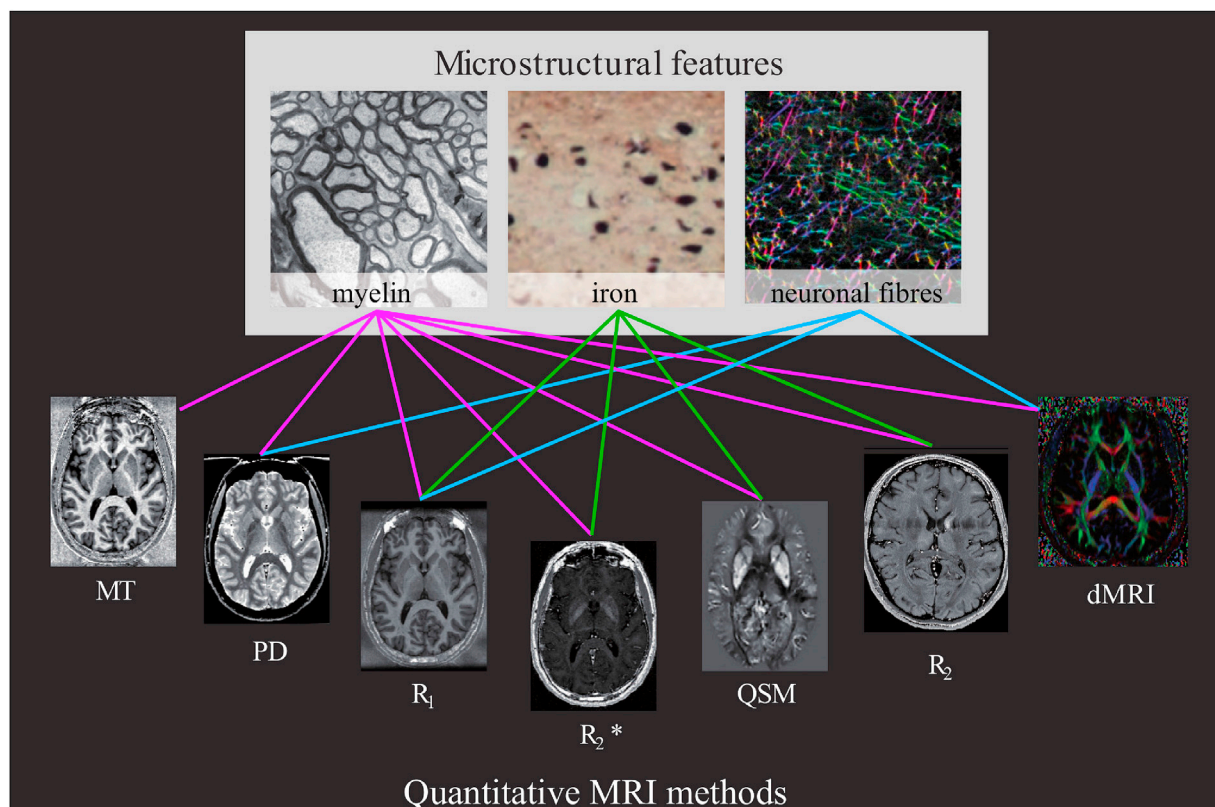


Fig. 3. Schematic representation of connections between MRI methods and the neocortical microstructural features reviewed in the text. A coloured line between a method and a microstructural feature implies that this method has been used to probe this feature in the reviewed papers in Sections [Myelin mapping: myeloarchitecture in vivo – Iron mapping: from glial cells to senile plaques](#). The relationships between MR contrast and microstructural features open the way to microstructural mapping through the combination of complementary quantitative MR images. The existence of a line between a microstructural substrate and an MRI method does not necessarily imply that the dependence is strong, and the absence of a line should not be taken to imply confirmation of no dependence. Microstructural features outside of those shown here can impact the contrast in MR images (examples may be found in Section [Other biological substrates and MR methods](#)), but are not included in the schematic for reasons of clarity. The indirect dependence of MR contrast on neuronal fibres via their orientational distribution with respect to B_0 is not explicitly represented here.

Table 1

Reviewed articles that used a single anatomical MRI contrast method (excluding dMRI, which is covered in Table 3) to make inferences about myelin (My) and iron (Fe) microstructure in the human neocortex. Anatomical images collected only for the purposes of segmenting cortical grey matter from other brain tissues and fMRI acquisitions have been omitted from the “MR modality” column, but are mentioned in the “Remarks” column where relevant. ✓ denotes that the authors interpreted their results in terms of that biological substrate and ? denotes that the authors stated their results could be affected by that biological substrate.

Reference	Biological substrate		MR modality	Resolution (mm ³)	B ₀ /T	Subjects	Remarks
	My	Fe					
Acosta-Cabronero et al. (2016)	✓		single-orientation QSM	1 × 1 × 2	3	116 subjects (20–79 y)	Used QSM to map age-related changes in the iron content of the brain. Strong age-related changes were found across diverse cortical areas, including the sensorimotor cortex, in line with known histology.
Buijs et al. (2017)	✓		T ₂ * w phase	0.24 × 0.24 × 1	7	70 subjects (22–80 y)	Examined age related changes in iron content in a priori defined cortical regions using maps of signal phase as a biomarker. Age-related changes were consistent with histological literature on cortical iron deposition in these regions.
Cohen-Adad et al. (2012)	✓	?	T ₂ *	0.33 × 0.33 × 1	7	8 subjects	Investigated cortical microstructure using T ₂ *. Found resemblance to classical parcellations in T ₂ *, and dependence of T ₂ * on orientation with respect to B ₀ in highly myelinated cortical regions.
De Martino et al. (2015)	✓		T ₁ w/T ₂ * w	0.6 × 0.6 × 0.6	7	6 subjects	Maps of T ₁ w/T ₂ * w showed consistent contrast with other MRI-based myelin mapping techniques. Combined myelin mapping with tonotopic fMRI (3 subjects), found heavily myelinated region in auditory cortex could correspond to primary auditory cortex in monkey.
Dick et al. (2012)	✓		T ₁	0.8 × 0.8 × 0.81	3	6 subjects	Myelin maps from T ₁ in auditory cortex were combined with fMRI tonotopic localisation of auditory areas. A small area was found at the group level (and in most subjects at the single-subject level) that had a similar cortical profile, orientation and shape to the ‘auditory core’ known from non-human primate and human ex vivo investigations.
Dinse et al. (2015)	✓		T ₁	0.5 × 0.5 × 0.5	7	9 subjects	Developed a T ₁ cortical myelin contrast model based upon cytoarchitecture that generated cortical profiles. Cortical-area specific signatures were found, with agreement between in vivo T ₁ cortical profiles and the model predictions. Validated using visual comparison to MRI of ex vivo sample at higher resolution and histological myelin stains.
Dumoulin et al. (2017)	✓		T ₁ w	0.5 × 0.5 × 0.5	7	4 subjects	T ₁ w images optimised for myelin contrast could differentiate striped-subdivisions in V2 and V3, as known from fMRI studies and invasive primate studies. These subdivisions corresponded well with subdivisions from fMRI performed in the same subjects.
Glasser et al. (2016)	✓	?	T ₁ w/T ₂ w	0.7 × 0.7 × 0.7	3	449 subjects	Used a combination of task-based and resting-state fMRI and T ₁ w/T ₂ w data to semi-automatically segment cortical architecture in a large group. Delineated 180 distinct cortical areas per hemisphere. Cross-validation, reproducibility, etc. evaluated by separating subjects into independent groups. Previous work suggested measure could also show some iron contrast (Glasser and Van Essen, 2011).
Huntenburg et al. (2017)	✓		T ₁	0.5 × 0.5 × 0.5	7	9 subjects	Found a systematic relationship between microstructural variations reflected in T ₁ (reflecting intracortical myelin) and resting state fMRI functional connectivity measures. Consistent with histological studies in mammalian species.
Kim and Knösche (2016)	✓		T ₁	0.7 × 0.7 × 0.7	7	8 AP musicians, 9 controls	Investigated regional differences in myelin density (throughout cortical depth) using T ₁ between musicians with absolute pitch (AP) and control subjects. Found a region with greater intracortical myelination compared to controls, with myelination correlating with a behavioural index of AP.
Kuehn et al. (2017)	✓		7 T: T ₁ , T ₂ * (one subject), group: T ₁ w/T ₂ w	7 T: 0.5 × 0.5 × 0.5, group: 0.7 × 0.7 × 0.7	7 T: 7, group: 3	7 T: 7 subjects, group: 440 subjects	Found a border of reduced myelin density between the functional hand and face areas in S1 and M1 using myelin-sensitive MR contrast in a large group, similar to known borders in rodent and monkey. The border coincided with borders defined using resting state fMRI. At 7 T this border could be found at the single subject level in T ₁ and T ₂ *, and was found to be cortical-layer specific.
Kwan et al. (2012)	✓		T ₂ *	0.31 × 0.31 × 1	7	5 ALS patients, 3 controls	Investigated cause of hypointensities in ALS lesions seen in T ₂ w images collected at 3 T as part of the same study. 7 T analysis was used to localise hypointensities to the deeper layers of the motor cortex. Comparison with ex vivo investigations led to the conclusion that the hypointensities were driven by paramagnetic iron-containing activated microglial cells.
Lifshits et al. (2018)	✓		multicompartment R ₁	7 TIs: 0.43 × 0.43 × 1.5, 107 TIs: 3 × 3 × 3	3	7 TIs: 15 subjects, 107 TIs: 18	Tested whether recording R ₁ w images at more inversion times (TIs) at a lower resolution could allow discrimination of R ₁ values corresponding to individual layers (by allowing multicompartment modelling) better than a higher resolution scan with less TIs (fit to just a single relaxation time). Results implied that R ₁ values corresponding to individual cortical layers could potentially be better evaluated with more TIs than with higher resolution acquisitions. Also evaluated method in ex vivo rat brain at higher resolution.
Rowley et al. (2017)	✓		T ₁ w/PDw	1 × 1 × 1	3	67 subjects (17–45 y)	Examined age-related changes in the cortical profile of the myelin marker T ₁ w/PDw. Found that the age-dependence could be well modelled using quadratic functions, and was region dependent. Parcellated cortex based upon age-dependence of myelin marker.
Sereno et al. (2013)	✓		R ₁	0.8 × 0.8 × 0.81	3	6 subjects	R ₁ cortical profiles matched known histological myelin laminar dependence. R ₁ maps showed borders between different visual cortices matching those defined functionally using fMRI.

(continued on next page)

Table 1 (continued)

Reference	Biological substrate		MR modality	Resolution (mm ³)	B ₀ /T	Subjects	Remarks
	My	Fe					
Shafee et al. (2015)	✓		Group: T ₁ w/T ₂ w, HR: T ₁ w	Group: 1.2 × 1.2 × 1.2, HR: 0.5 × 0.5 × 0.5	3	Group: 1555 subjects (18–35 y) HR: 5 subjects	Demonstrated that correcting for partial volume effects is essential for obtaining unbiased myelin markers, validated by comparison to high resolution (HR) scans and an ex vivo 7 T scan at finer resolution. Group showed increase of T ₁ w/T ₂ w values with age, reflecting increases in myelination. Inner cortical layers appeared more myelinated than outer layers, and the age dependent increase in myelination was mainly reflected in the inner layers.
Wachnert et al. (2016)	✓		T ₁	0.5 × 0.5 × 0.5	7	9 subjects	Myeloarchitectonic maps were computed from T ₁ at different cortical depths; unfortunately were insufficient to generate single subject maps. Profiles accurately reflected T ₁ myeloarchitecture as found by comparing to finer resolution MRI image of ex vivo tissue and examining manually delimited V1. Effect of curvature shown to be minimised by their choice of coordinate system.
Whitaker et al. (2016)	✓		MTsat	1 × 1 × 1	3	297 subjects (14–24 y)	Used MRI to demonstrate that cortical increases in myelination and cortical shrinkage during adolescence are concentrated at “hubs” in the cortex. Cortical thickness was determined from simultaneously acquired R ₁ maps. MTsat used as myelin marker because more specific than R ₁ .
Zhao et al. (2016)		✓	multicompartment R ₂ [*]	1 × 1 × 2	3	20 subjects (22–74 y)	Decomposed R ₂ [*] contrast into contribution from tissue and from vasculature. Found that the tissue contribution to R ₂ [*] increased with age, possibly reflecting cellular packing density. Found different rates of age-related increase in different cortical areas.

also been excluded. We focus on the current state-of-the-art, omitting earlier proof-of-concept studies. An overview of the reviewed articles is given in Tables 1–3.

Quantitative MRI and its relationship to hMRI

Many of the articles we review below make use of quantitative MRI (qMRI) methods. These methods combine traditional “weighted” MR images in a model-based fashion to give maps of “quantitative” values that are more reproducible (Weiskopf et al., 2013; Govindarajan et al., 2015; Feng et al., 2018) and more independent of acquisition scheme (Stikov et al., 2015) than weighted images.

The models used to generate quantitative maps are usually relatively simple physical models, several of which are described below. These models are formally exact when the underlying model assumptions are met (e.g. longitudinal relaxation is a monoexponential magnetization recovery process described by a single relaxation rate R₁), but should fail relatively gracefully when these assumptions do not hold (e.g. a voxel containing several tissue components with different R₁ values can give rise to multi-exponential behaviour that is still captured by a single approximately acquisition-independent effective R₁ value (Fullerton et al., 1982)). The cortex represents a very complex physical system probed with relatively noisy measurements; such models represent necessary simplifications.

For the purposes of hMRI, it is important to relate the values in quantitative maps to the underlying tissue microstructure. This can be achieved in two ways. The first is to determine a mapping between aspects of tissue microstructure and quantitative parameters (e.g. voxel-wise myelin content appears to be proportional to the measured R₁ value; see Section Myelin mapping: myeloarchitecture in vivo). The second is to build a simplified physical model of the tissue microstructure which allows extraction of microstructurally-relevant quantitative maps directly. This second approach is relatively common when applying hMRI to neuronal fibre microstructure; see Section Neuronal fibre mapping: intracortical connectomics.

We now briefly summarise the quantitative methods that are utilised in the rest of this review. For the sake of brevity, many details of the models and assumptions are not covered here; these details are contained in the cited literature.

An important set of quantitative imaging methods arise from the field of relaxometry (Does, 2018). The longitudinal relaxation time (T₁) describes the characteristic time of energy dissipation in a spin system, and is sensitive to interactions of water molecules with other water molecules (Abragam, 1961), water molecules bound to macromolecules (Koenig, 1991; Leuze et al., 2017), and the paramagnetic centres (Abragam, 1961) found in cortical tissue (Stüber et al., 2014; Yablonskiy and Sukstanskii, 2017; Duyn and Schenck, 2017). The transverse (T₂; MacKay et al., 2006; Laule et al., 2007) and effective transverse (T₂^{*}; Govindarajan et al., 2015; Yablonskiy and Sukstanskii, 2017; Duyn and Schenck, 2017) relaxation times are both strongly sensitive to the small magnetic fields induced by the scanner's strong main magnetic field (B₀) in diamagnetic and paramagnetic tissue components (e.g. paramagnetic iron). Additionally, magnetization transfer (MT) reflects exchange between fast relaxing water bound to macromolecules and slowly relaxing unbound water molecules (Pike, 1996; Stanisiz et al., 1999), and can be harnessed to extract parameters that depend strongly on the macromolecular content of tissue (Schmierer et al., 2004; Sled, 2018). In the following, relaxation times (T_N) and relaxation rates (R_N = 1/T_N) are used interchangeably as needed.

Proton density (PD) reflects the MR-visible water content of a voxel (Tofts, 2004b), and decreases as the density of MR-invisible macromolecules (e.g. lipids and proteins) in a voxel increases (Mezer et al., 2013; Gomez et al., 2017).

The phase of the complex-valued MR signal is also sensitive to the small magnetic fields induced in diamagnetic and paramagnetic tissue

Table 2

Reviewed articles that used a combination of anatomical MRI contrast methods (excluding dMRI, which is covered in Table 3) to make inferences about myelin (My), iron (Fe), and neuronal fibre (Neu) microstructure in the human neocortex. Anatomical images collected only for the purposes of segmenting cortical grey matter from other brain tissues and fMRI acquisitions have been omitted from the “MR modality” column, but are mentioned in the “Remarks” column where relevant. ✓ denotes that the authors interpreted their results in terms of that biological substrate and ? denotes that the authors stated their results could also be affected by this substrate.

Reference	Biological substrate			MR modality	Resolution (mm ³)	B ₀ /T	Subjects	Remarks
	My	Fe	Neu					
Allen et al. (2017a)	✓	✓		R ₁ , MTsat, R ₂ [*]	0.8 × 0.8 × 0.8	3	48 subjects	Found the myelin marker MTsat correlated with differences in a measure of cognitive empathy in the insular cortex, and that the iron marker R ₂ [*] predicted a measure of affective empathy in the secondary somatosensory cortex.
Allen et al. (2017b)	✓	✓		R ₁ , MTsat, R ₂ [*]	0.8 × 0.8 × 0.8	3	48 subjects	Found relationships between measures of a metacognitive ability and microstructural markers. Greater ability corresponded to higher myelination (evaluated with R ₁ and MTsat) in anterior prefrontal cortex, lower iron levels (evaluated with R ₂ [*]) in visual cortex, and higher iron levels in the precuneus.
Betts et al. (2016)	?	?		R ₂ [*] , single orientation QSM	0.8 × 0.8 × 1.6	7	20 younger adults, 20 older adults	Regional age related R ₂ [*] and QSM changes found in cortex. Confirmed that atrophy and head position were not the reason for the apparent effects. Differential R ₂ [*] and QSM effects suggest might be able to probe effects of iron and myelin separately.
Callaghan et al. (2014)	✓	✓		R ₁ , R ₂ [*] , MTsat, effective PD	1 × 1 × 1	3	138 subjects (19–75 y)	Used R ₂ [*] as an iron marker, and R ₁ and MTsat as myelin markers. Characterised the spatial distribution of normal-ageing related changes in the brain, including cortex. Found wide-spread cortical age-related changes in all markers. Differential age-related contrast changes between markers allowed for tentative distinction between demyelination and iron deposition.
Costagli et al. (2016)		✓		T ₂ [*] w, single orientation QSM	0.25 × 0.25 × 2, 0.5 × 0.5 × 1	7	17 ALS patients, 13 controls	Investigated layer specific QSM and T ₂ [*] w contrast in subjects with ALS and healthy controls in M1. Higher resolution acquisition targeted M1 explicitly. Susceptibility correlated with expected iron burden in ALS subjects and healthy controls, and susceptibility correlated with clinical scores of ALS impairment. Increased susceptibility colocalised with T ₂ [*] w hypointensity in deeper cortical layers, suggesting contrast could be due to activated microglia.
Deistung et al. (2013)	?	?		R ₂ [*] , multi-orientation QSM	R ₂ [*] : 0.8 × 0.8 × 0.8, QSM: 0.4 × 0.4 × 0.4	7	9 subjects	Suggested myelin is the main contributor to grey matter–white matter contrast, while iron is most responsible for differences between cortical areas. The low resolution of their R ₂ [*] maps limited their ability to disentangle laminar iron and myelin contributions. QSM maps showed laminar variations consistent with known histology.
Fukunaga et al. (2010)		✓		R ₂ [*] (only ex vivo), R ₂ [*] w, phase	ex vivo: 0.15 × 0.15 × 0.15, 0.13 × 0.13 × 0.5, 0.08 × 0.08 × 0.5, in vivo: 0.24 × 0.24 × 1.0	7	1 subject, ex vivo tissue blocks	Examined laminar variation of phase and R ₂ [*] contrast reflecting iron and myelin content in ex vivo tissue from occipital and parietal cortex. Found iron extraction strongly reduced contrast, implying iron content explains most of the intracortical MRI contrast. Found colocalisation of iron and myelin using histology. Contrast variations consistent with ex vivo investigation were also demonstrated in an in vivo acquisition.
Gomez et al. (2017)	?		?	T ₁ , PD	0.8 × 0.8 × 1	3	25 adults, 22 children	Contrasted tissue differences between adults and children in face- and place-selective cortical areas known to only be microstructurally differentiated in adults. Regions of interest were determined using fMRI. Argued effects in PD and T ₁ too large to be explained by myelin changes. By contrasting PD and T ₁ maps, showed changes between children and adults likely due to proliferation of macromolecules besides myelin, possibly reflecting dendrite or glial cell proliferation.
Haast et al. (2016)	✓			R ₁ , T ₁ w, T ₂ [*] , T ₁ w/T ₂ [*] w, R ₁ /T ₂ [*]	0.7 × 0.7 × 0.7	7	10 subjects	Found quantitative R ₁ to be best parameter to map the cortical myelin distribution in vivo. This was determined via comparison of measures such as cortical ‘parcellability’, CNR, and (intra- and inter-subject) variability and reproducibility between the quantitative parameters and their weighted counterparts.
Helbling et al. (2015)	✓			R ₁ , R ₂ [*] , MTsat	0.8 × 0.8 × 0.8	3	5 subjects	Myelin mapping of the auditory cortex using multiple relaxometry parameters predicted the origin of MEG signals in an auditory task, implying structure–function relationship. R ₁ was found to be the best predictor.
Mangeat et al. (2015)	✓	?		R ₂ [*] , MTR	R ₂ [*] : 0.33 × 0.33 × 1, MTR: 1.2 × 1.2 × 1.2	R ₂ [*] : 7, MTR: 3	7 subjects	Found high correlation between MTR and T ₂ [*] over whole cortex, reflecting a common contrast source; assumed this source is myelin. Combined MTR and T ₂ [*] images by using independent component analysis after using multilinear regression to account for B ₀ -orientation and cortical thickness dependence of the parameters (though the effect of these two confounds was found to be relatively small). Found combined contrast more closely reflected the distributions in classical myelin stains than in iron stains.
Marques et al. (2017)	✓	✓		R ₁ , R ₂ [*] , multi-orientation QSM	R ₁ : 0.6 × 0.6 × 0.6, R ₂ [*] , QSM: 0.66 × 0.66 × 0.66	7	6 subjects	Used a linear model to disentangle myelin and iron MR contrast contributions to cortical profiles of qMRI maps in several atlas-based cortical regions. Iron map appeared to show the most contrast between cortical regions, but linear model fit was not good over all cortical areas and depths.

(continued on next page)

Table 2 (continued)

Reference	Biological substrate			MR modality	Resolution (mm ³)	B ₀ /T	Subjects	Remarks
	My	Fe	Neu					
Sánchez-Panchuelo et al. (2012)	✓			T ₁ w, T ₂ *w	T ₂ *w: 0.4 × 0.4 × 0.4, T ₁ w: 0.6 × 0.6 × 0.6	7	4 subjects	Singular value decomposition over cortical depth gave contrast that could lead give better parcellation than the individual qMRI maps. T ₂ *w contrast used to investigate myelinated bands in cortex. Optimal contrast determined using quantitative imaging in a pilot study. Studied correspondence of the position of banded regions in T ₂ *w images with V1 and V5/MT on the single-subject level, the locations of which were determined using fMRI. Good overlap was found for V1, but not for V5/MT. T ₂ *w images were found to show myelinated bands more clearly.
Stüber et al. (2014)	✓	✓		R ₁ , R ₂ *, single orientation QSM	0.1 × 0.1 × 0.1, 0.2 × 0.2 × 0.2	7	ex vivo tissue blocks	Disentangled contributions of iron and myelin to the recorded MR images ex vivo with the help of advanced histological techniques and linear modelling.
Wasserthal et al. (2014)	✓			T ₁ w, T ₂ w	0.7 × 0.7 × 0.7	3	39 subjects	Segmented highly myelinated human primary auditory cortex at the single subject level, using an automatic method to combine the T ₁ w and T ₂ w data. Found evidence of a secondary highly myelinated area outside the probability map for primary auditory cortex.

components by B_0 . MR signal phase can thus be used to make inferences about the magnetic susceptibility of the tissue, especially when localised to the source of the phase disturbance using quantitative susceptibility mapping (QSM) techniques (Yablonskiy and Sukstanskii, 2017; Duyn and Schenck, 2017).

The cell membranes and myelin sheaths of neuronal fibres (Fig. 1h–j) restrict and hinder the diffusion of MR-visible water molecules (Alexander et al., 2018). Furthermore, the anisotropic nature of the fibres and their anisotropic orientation distribution conspire to make water diffusion in cortex anisotropic (Jespersen et al., 2007; Beaulieu, 2011). Diffusion MRI (dMRI) allows us to probe this anisotropic diffusion in an orientation specific way (Callaghan, 1993; Bassler and Özarslan, 2011), giving orientation specific insights into the tissue microstructure that are not easily accessible using other MRI techniques.

In addition to the qMRI methods described above, Tables 1 and 2 show that non-quantitative images have also been used to gain insight into topics of neuroscientific and clinical interest. Non-quantitative images can achieve optimal contrast-to-noise ratio (CNR) per unit time between selected sets of cortical features, e.g. between white and grey matter (Deichmann et al., 2000), between cortical layers (Trampel et al., 2011; Sánchez-Panchuelo et al., 2012), or between cortical areas (Van Essen et al., 2012; Glasser et al., 2013). Therefore, for a subset of specific neuroscientific and clinical questions, collection of non-quantitative data may be sufficient. Importantly, this can allow for shorter acquisition times—an essential consideration in studies of clinical populations.

Decreases in acquisition time afforded by non-quantitative imaging must, however, be weighed against the loss of the advantages of quantitative metrics discussed above.

The loss of these advantages is particularly apparent as one moves to higher magnetic field strengths, where the intensity of the transmitted radiofrequency (RF) magnetic field becomes very inhomogeneous over the brain (Lutti et al., 2014; Bazin et al., 2014). This inhomogeneity means that the CNR can only be optimised over relatively small areas (e.g. over a lobe of the brain). Heuristic methods developed at 3 T to correct for bias in the RF receive and transmit sensitivity (e.g. Glasser and Van Essen (2011)) cannot correct for this higher RF transmit bias at higher magnetic field strengths. It is to a large extent for this reason that qMRI methods are to be preferred for cortical segmentation (Bazin et al., 2014) and parcellation (Haast et al., 2016) at 7 T and above. For the purposes of parcellation or segmentation, collection of quantitative data gives scope for the generation of synthetic images with optimal CNR (Nöth et al., 2015; Callaghan et al., 2015a, 2016; Lorio et al., 2016) which are much less affected by the transmit inhomogeneity.

It is our opinion that for the purposes of hMRI, sufficient data to compute qMRI maps should be collected wherever possible, as this can allow more specific and reproducible microstructural inferences to be made from the data, as already demonstrated in some clinical studies (e.g. Freund et al. (2013)). An important branch of qMRI method development thus lies in trying to overcome the present limitations of qMRI techniques (e.g. Weiskopf et al. (2013); Metere et al. (2017)). This includes making use of advances such as compressed sensing (Lustig et al., 2007, 2008) and the extensive use of parallel imaging (Blaimer et al., 2004; Larkman and Nunes, 2007; Setsompop et al., 2016; Hamilton et al., 2017) to allow reductions in the scan times needed for qMRI.¹ However, determination of the optimal protocol for a given study must

¹ For example, multiparameter mapping of R_1 , R_2^* , and semi-quantitative PD has been achieved in ~ 19 minutes using a 3 T scanner at an isotropic voxel resolution of 800 μ m (Callaghan et al., 2015b; Allen et al., 2017a; b; Ellerbrock and Mohammadi, 2018b). This scan-time was split between acquiring two weighted datasets (~ 7 minutes each) and acquiring calibration data (~ 5 minutes total). This compares favourably to the ~ 13 minute-long non-quantitative 800 μ m 3 T Lifespan protocol acquired as part of the Human Connectome Project (<https://www.humanconnectome.org/lifespan-studies>; Van Essen et al., 2012; Glasser et al., 2013).

Table 3

Reviewed articles that used diffusion MRI to make inferences about myelin (My) and neuronal fibre (Neu) microstructure in the human neocortex. Most studies also collected anatomical images for the purposes of segmenting cortical grey matter from other brain tissues which are not explicitly mentioned here. DTI: diffusion tensor imaging (Basser and Özarslan, 2011), FWE-DTI: free water elimination-DTI (Pasternak et al., 2009), HARDI: high angular resolution diffusion imaging (Farquharson and Tournier, 2016), MSMT-CSD: multishell multitissue-constrained spherical deconvolution (Jeurissen et al., 2014), NODDI: neurite orientation dispersion and density imaging (Zhang et al., 2012). ✓ denotes that the authors interpreted their results in terms of that biological substrate and ? denotes that the authors stated their results could also be affected by this substrate.

Reference	Biological substrate		acquisition/model	Resolution (mm ³)	B ₀ /T	Subjects	Remarks
	My	Neu					
Aggarwal et al. (2015)	✓	✓	HARDI	0.09 × 0.09 × 0.09	11.7	12 ex vivo tissue blocks	A proxy for tangential fibre density was consistent with laminar structure of myelin stains in tissue blocks from four distinct cortical areas. Radial anisotropy in upper layers suggested also sensitive to dendrites. Tractography was used to differentiate tangential and radial fibre densities.
Calamante et al. (2018)	✓	✓	MSMT-CSD	1.25 × 1.25 × 1.25	3	8 subjects	Generated an apparent fibre density metric from spherical expansion of diffusion signal accounting for partial volume effects. Found similar differences between cortical areas as found using myelin mapping techniques; could permit cortical parcellation. Radiality metrics reproduced results of McNab et al. (2013).
Kleinnijenhuis et al. (2015)		✓	DTI	1 × 1 × 1	7	5 subjects	Analysed diffusion parameter maps along cortical profiles to examine effect of cortical curvature on diffusion parameters, including a proxy for the radiality of the neuronal fibre orientation distribution. Radiality varied with cortical curvature, which is consistent with ex vivo histology.
Leuze et al. (2014)	✓	✓	HARDI	0.24 × 0.24 × 0.24	9.4	3 ex vivo tissue blocks	Used dMRI to probe cortical profiles of the neuronal fibre distribution using tractography in tissue blocks containing the border between V1 and V2. Found preferential V1–V2 connections in upper cortical layers in both dMRI and histological stains for myelin.
McNab et al. (2013)	✓	✓	DTI	1 × 1 × 1	3	6 subjects	Found diffusion tensor in M1 is more radial relative to the cortical normal than the diffusion tensor in S1. Similar differences were found in other regions of cortex. Validated by imaging ex vivo tissue and an anaesthetized macaque at higher resolutions.
Morris et al. (2016)		✓	NODDI	2 × 2 × 2	3	38 subjects	Investigated neuronal fibre density in regions associated with behaviour. Showed that increases in a diffusion-derived metric related to neuronal fibre complexity in a functionally defined cortical area in the medial orbitofrontal cortex (mOFC) were correlated with increases in model based decision making.
Nagy et al. (2013)	?	?	HARDI	2.3 × 2.3 × 2.3	3	3 subjects	Parcellated the cortex using (model free) feature extraction from diffusion data.
Nazeri et al. (2015)		✓	NODDI	2 × 2 × 2	3	45 subjects (21–84 y)	Found widespread decreases in cortical neuronal fibre orientation dispersion (OD) with increasing age, especially in frontoparietal cortex. Found correlations between cortical OD and measures of cortical connectivity from resting-state fMRI at the nodes of several resting-state networks in the cortex. Speculated that changes could be related to known changes in dendritic morphology with age.
Rathi et al. (2014)	?	✓	FWE-DTI	1.7 × 1.7 × 1.7	3	85 subjects (15–55 y)	Examined age-related cortical changes using a non-standard measure of DTI-parameter deviation that they called “tissue heterogeneity” within regions of interest. Found significant age related increases in this heterogeneity measure in the frontal and parietal lobes, in line with models of ageing from the functional, cognitive, and structural domains.

still be carried out on a case-by-case basis, making the appropriate trade-off between CNR, scan-time, specificity, and image artefacts, taking into account the specific aims and scope of the study.

Challenges of cortical MRI

In vivo imaging of human neocortex is challenging for a number of reasons. Human neocortex is very thin (1.6 mm–4.5 mm; von Economo and Koskinas, 1925; Fischl and Dale, 2000; Scholtens et al., 2015; Glasser et al., 2016) and strongly gyrified to a highly subject specific extent (Ono et al., 1990). It can also be hard to segment cortex from the underlying white matter in regions where cortex is highly myelinated (Scholtens et al., 2015; Lorio et al., 2016). Further, the neocortical regions of MR images are strongly affected by partial volume effects due to the proximity of cortex to cerebrospinal fluid (CSF), white matter, and vasculature, and are plagued by artefacts (including those arising from

susceptibility differences, subject motion, and Gibbs ringing) that are especially prevalent due to the presence of sharp borders between cortex and white matter/CSF.

Means of mitigating these problems have been reviewed elsewhere (Deistung et al., 2013; Bazin et al., 2014; Cohen-Adad, 2014; Weiskopf et al., 2015; Waehnert et al., 2016; Lorio et al., 2016; Lerch et al., 2017), and so will not be covered explicitly here. We note, however, that these problems drive the use of layer based analyses (Bazin et al., 2014; Cohen-Adad, 2014; Waehnert et al., 2016; Weiskopf et al., 2015), hardware such as prospective motion correction systems (Callaghan et al., 2015b) and ultra high field strength scanners (Stucht et al., 2015) which allow for high resolution acquisitions, and lead to a preference for multiparameter acquisitions that do not require extensive coregistration (Callaghan et al., 2015b; Weiskopf et al., 2015; Lorio et al., 2016; Metere et al., 2017).

We mention these challenges to ensure that readers take them into

account when carrying out their own studies.

Myelin mapping: myeloarchitecture in vivo

Following the previous two technical subsections, we now move our focus to the mapping of three microstructural components of the cortex: myelin, iron, and neuronal fibres. Each section is organised into three parts. We first describe MRI techniques that have been used to detect a given component, discussing each technique in terms of its sensitivity and specificity. We follow this with a review of the neuroscientific and clinical applications of mapping this component in the literature. We then provide a brief summary to close each subsection.

MRI techniques

Microstructural interactions of water with the myelin sheath and its biochemical components impact the mesoscopic MRI signal in several ways. Interactions between water molecules and the biomolecular components (mainly lipids (Kucharczyk et al., 1994), among them cholesterol (Koenig, 1991)) of myelin affect the spin-relaxation of water, causing changes in T_1 (Koenig, 1991), T_2 (Laule et al., 2007; Knight and Kauppinen, 2016; West et al., 2018), T_2^* (Wharton and Bowtell, 2012; Chen et al., 2013; Jung et al., 2018), and related MT-based metrics (Laule et al., 2007; West et al., 2018) on the meso- and macroscopic scales, reflecting differences in myelin density and distribution. Myelin also has a diamagnetic susceptibility; myelin thus gives rise to contrast in signal-phase and QSM maps (Wharton and Bowtell, 2012; Deistung et al., 2017; Duyn and Schenck, 2017; Duyn, 2017; Yablonskiy and Sukstanskii, 2017; Xu et al., 2018). An increase in myelin density also reduces PD (Mezer et al., 2013; Berman et al., 2018). In addition, contrast in dMRI at least partially reflects myelin content (Leuze et al., 2014; Aggarwal et al., 2015; Kleinnijenhuis et al., 2015), however we consider dMRI separately in Section [Neuronal fibre mapping: intracortical connectomics](#).

The relatively complex internal structure of myelin and the orientated nature of the myelinated fibres give rise to an orientation dependence with respect to B_0 of the image contrast of maps of T_2 (Gil et al., 2016; Knight and Kauppinen, 2016), T_2^* (Cohen-Adad et al., 2012), QSM (Wharton and Bowtell, 2012), and MT (Pampel et al., 2015). However, when modelling these orientation effects it should be taken into account that most models of these orientation-dependences were developed with highly-orientated white matter fibre bundles in mind, rather than the more orientationally-dispersed myelinated fibres in cortical grey matter.

Based on the above, it is in principle possible to map correlates of microscopic myeloarchitecture at the macroscopic and mesoscopic scale using parameters from relaxometry, QSM, and PD as proxies for myelin content. There are, however, several caveats.

MT contrast is fairly specific to myelin content in healthy tissue (Laule et al., 2007), but obtaining quantitative metrics while maintaining a reasonable measurement time is challenging (Campbell et al., 2018). Nevertheless, semi-quantitative metrics have been developed that serve as useful myelin markers, such as the MT ratio (MTR; Tofts et al., 2004), MT saturation (MTsat; Helms et al., 2008), and other similar parameters (Laule et al., 2007; Campbell et al., 2018). It should be noted, however, that pathological processes unrelated to myelination can also affect these MT metrics (Vavasour et al., 2011).

Methods utilising T_2 images have been used to estimate myelin water volume fractions in brain (MacKay et al., 2006; Laule et al., 2007), but we are not aware of any studies that have applied this method in a laminar- or area-specific fashion in human cortex. This omission is at least partially due to the relatively small variation of T_2 -based myelin metrics in cortex (Zhang et al., 2015), coupled with observations of comparably large errors in cortical parameter estimates due to CSF contamination (Meyers et al., 2017).

PD has been shown to be sensitive to white matter myelin content (Mezer et al., 2013; Berman et al., 2018). However, an investigation by Gomez et al. (2017) of maturation-related cortical PD change in a functionally-derived cortical area found a decrease in PD with age that

seemed too large to be exclusively due to an increase in myelination. They speculated that this change could instead be driven by processes such as dendrite or glial cell proliferation. Interestingly, Gomez et al. (2017) implied that their observed T_1 decrease with age could also be driven by this process, rather than by myelination (see Sections [Neuronal fibre mapping: intracortical connectomics](#) and [Other biological substrates and MR methods](#)).

T_1 , T_2^* and QSM images are also influenced by paramagnetic iron, reducing their specificity. The variation of T_1 values over the cortex is, however, more strongly dependent on myelin concentration than on iron concentration (Stüber et al., 2014; Leuze et al., 2017; Morawski et al., [this special issue](#)), making this a relatively sensitive and specific marker for changes in myelin content (Dick et al., 2012; Sereno et al., 2013; Lutti et al., 2014; Campbell et al., 2018).

The non-specificity of contrast in T_1 , T_2^* and QSM images with respect to myelin and iron can in principle be alleviated by combining complementary quantitative images using a model to extract independent iron and myelin maps. Ex vivo investigations have demonstrated the potential of this approach, with Stüber et al. (2014) showing that a linear model can extract iron and myelin maps from a combination of T_1 , T_2^* , and QSM images. However, in vivo application has had less success; Marques et al. (2017) found that translation of the linear model to the in vivo case resulted in physiologically inconsistent iron and myelin maps, which suggests that changes are required for the model to be applied in vivo. One explanation is that perhaps the linear model only functions in the primary cortical areas examined by Stüber et al. (2014). Alternatively, it could be due to biological contributions to the MR signal that have not been taken into account; the effects of vasculature (Ulrich and Yablonskiy, 2016; Zhao et al., 2017) would be one important contribution to investigate.

Applications

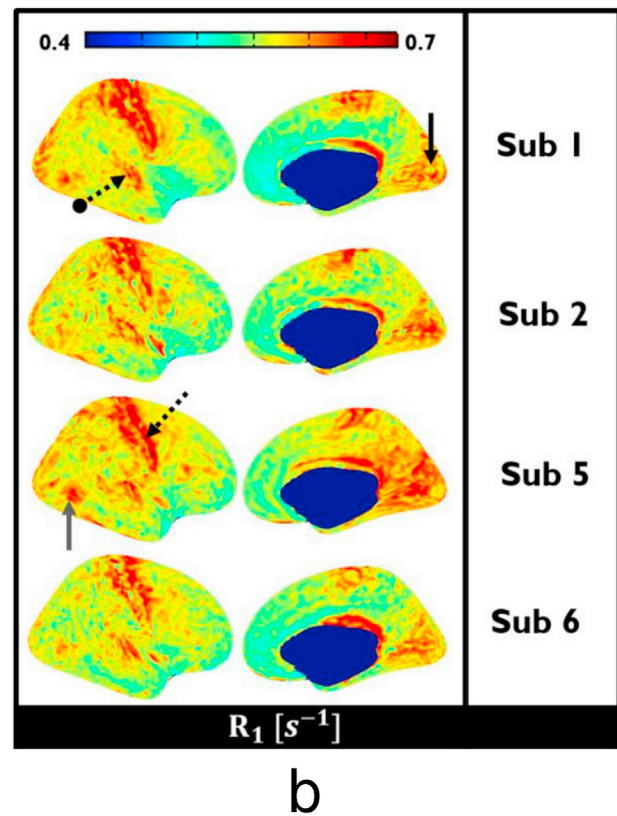
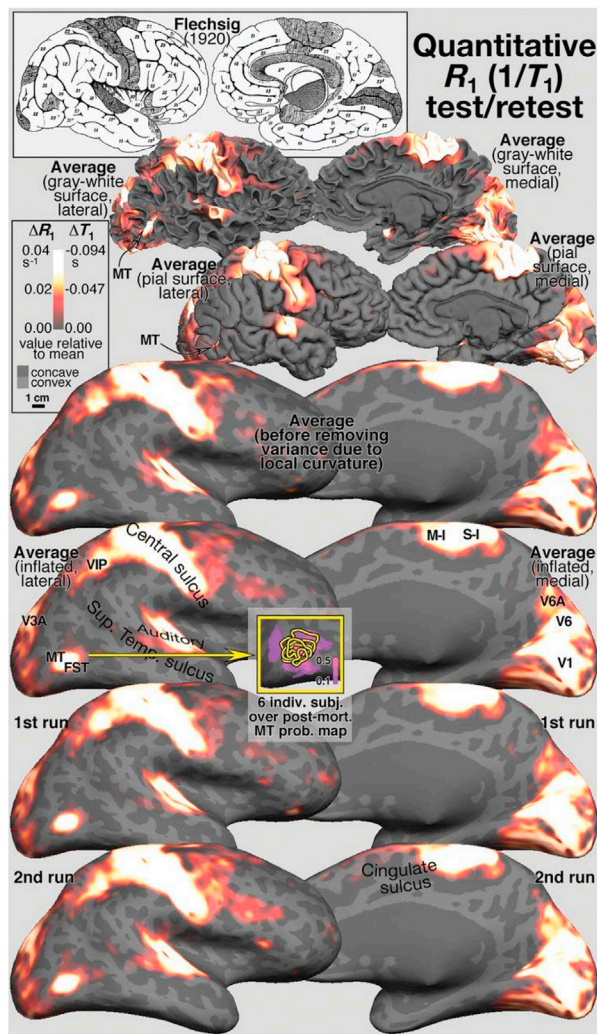
The main use of myelin mapping techniques in cortex has been in vivo parcellation into macroscopic myeloarchitectonic areas (Geyer et al., 2011; Dick et al., 2012; Sereno et al., 2013; Haast et al., 2016). Fig. 4 exemplifies why this is the case: highly myelinated sensory cortical areas can be clearly distinguished using in vivo MRI at the group (Dick et al., 2012; Sereno et al., 2013) and single-subject (Wasserthal et al., 2014; Haast et al., 2016; Marques et al., 2017) levels.

A concrete example of myeloarchitectonic parcellation is a recent study by Glasser et al. (2016), who found that combining a heuristic myelin marker (a T_1 -weighted image divided by a T_2 -weighted image) with task- and resting state-fMRI data in several hundred subjects allowed for the parcellation of each hemisphere into 180 cortical areas (see Fig. 1c). The combination with resting state fMRI measures further implies different functionality for the differentiated areas.

In a similar vein, studies utilising specific functional paradigms have searched for myelination differences corresponding to specific functional subdivisions. These include evidence of myelinated stripes purported to collocate with COx stripes in secondary visual cortex (Dumoulin et al., 2017), myelination differences corresponding to different body parts confirmed using task-based fMRI in primary motor and somatosensory cortex (Glasser et al., 2016; Kuehn et al., 2017), and differentiation between different auditory (Dick et al., 2012; De Martino et al., 2015; Kim and Knösche, 2016) and visual (Sánchez-Panchuelo et al., 2012; Sereno et al., 2013) cortical areas.

Combining quantitative images in a ‘model-free’ fashion can improve contrast for cortical parcellation. Mangeat et al. (2015) used independent component analysis to combine MTR maps with T_2^* maps, after mitigating the effect of cortical thickness and B_0 orientation-dependence on these parameters using multilinear regression. They found promising signs that the combined image is a more sensitive myelin marker than the individual maps.

Myelin mapping has also been used to investigate other questions of neuroscientific and clinical relevance. A proof-of-concept validation by



a

b

Fig. 4. R_1 maps allow for the differentiation of myeloarchitectonic areas. (a) Group average R_1 maps at 3 T show areas of high R_1 value consistent with classical myeloarchitectonic parcellations (such as the parcellation redrawn above the R_1 maps from Flechsigs (1920) showing the early myelinating areas) that are reproducible (reproduced from Sereno et al. (2013)). (b) Differentiation of myeloarchitectonic areas in R_1 maps is possible at the single subject level at 7 T. The solid black arrow points to primary visual cortex, the dashed arrow points to primary motor cortex, the dot-ended dashed arrow points to primary auditory cortex, and the solid grey arrow points to the middle temporal region (reprinted from Marques et al. (2017) with permission from Elsevier).

Helbling et al. (2015) found that in vivo myelin metrics could be useful in helping to localise magnetoencephalography (MEG) signals in auditory cortex, which would allow combination of the high temporal resolution of MEG with the high spatial localisation of MRI. Similarly, Huntenburg et al. (2017) used the differing T_1 values throughout the brain as a proxy for differing myelin microstructure, and found that, for unimodal functional cortical areas, similarity of areas according to this proxy was a good predictor for whether two areas were functionally connected.

Myelin maps have also been used to investigate the development of the neocortex with age. Whitaker et al. (2016) found, using MRI-based MT saturation and cortical thickness measurements, that changes in areas that they could associate with the development of schizophrenia were driven by myelogenesis during development. The age-dependence of myelination in adults has also been examined (Callaghan et al., 2014), including findings that intracortical myelin content can be treated as a quadratic function of age from late adolescence to middle adulthood (Rowley et al., 2017), and that the inner layers of cortex show the most increase in myelination with age (Shafee et al., 2015).

Although highly important neuroscientifically, many of the previously mentioned studies have the drawback that they either selected one central cortical surface or averaged over several central cortical surfaces. Studies making use of the whole cortical profile can incorporate more

mesoscopic information and thus allow parcellation in a manner more closely resembling classical myeloarchitectonic maps (Dick et al., 2012; Sereno et al., 2013; Dinse et al., 2015; Waehnert et al., 2016; Kim and Knösche, 2016), or allow one to narrow down which mesoscopic laminæ are associated with an observed change of neuroscientific relevance (Shafee et al., 2015; Whitaker et al., 2016; Rowley et al., 2017). Unfortunately, obtaining data with both sufficient signal-to-noise ratio (SNR) and sufficient resolution to perform laminar analysis over the whole cortex remains a challenge (Trampel et al., 2018). Recent work has, however, suggested that multi-compartment T_1 models could provide some of the same information as laminar analysis at lower nominal acquisition resolutions (Lifshits et al., 2018).

Summary

In vivo myelin mapping using MRI is becoming ever more established. Several myeloarchitectonic areas, especially primary cortical areas, can be robustly distinguished (Geyer et al., 2011; Dick et al., 2012; Sereno et al., 2013), and advances in laminar MRI promise the ability to distinguish even more (Dinse et al., 2015; Trampel et al., 2018). T_1 mapping has proven itself to be a robust method for cortical parcellation (Lutti et al., 2014; Haast et al., 2016). Combination of a myelin metric with fMRI techniques has been shown to allow the discrimination of even

more cortical areas (Glasser et al., 2016). The possible increase in specificity and sensitivity promised by the combination of multiple complementary quantitative maps remains an open area of investigation.

Neuronal fibre mapping: intracortical connectomics

MRI techniques

The diffusion length of water over the diffusion time scale that can be probed with MRI covers the micro- and mesoscopic scales (Novikov et al., 2016). Neuronal fibres (more specifically, axons and dendrites) are thought to be the major boundaries and hindrances to diffusion in cortex on these scales, providing a source of anisotropic cortical diffusion contrast (Jespersen et al., 2007, 2012; Zhang et al., 2012; Aggarwal et al., 2015; Alexander et al., 2018), though the observed anisotropy is much lower than that seen in white matter (D'Arceuil and de Crespigny, 2011). Through the use of appropriate models, the anisotropic diffusion contrast can be interpreted in terms of fibre orientation distribution functions and fibre densities. Because fibres oriented tangentially to the cortical surface mostly represent intralaminar connections and fibres oriented radially mostly represent interlaminar fibres or fibres leaving/entering the cortex (Section *Cortical architecture: what we want to see!*), knowing the density of fibres in a given orientation allows insights into connectivity more specific than the insights available from the myelin mapping methods described in Section *Myelin mapping: myeloarchitecture in vivo*.

The biological membranes and other chemical components of neuronal fibres can also contribute to observed contrast in other MR modalities. A concrete example can be found in Gomez et al. (2017), where it was argued that an observed decrease in PD was too large to be entirely due to increasing myelin content. On this basis, it was hypothesised that dendritic proliferation could be a possible cause of the observed change. This being so, it was further argued that the observed decrease in T_1 likely reflected the same process, and thus was (at least partially) driven by an increase in tissue lipid concentration associated with the proliferation of dendrites, rather than being exclusively driven by changes in myelination. However, despite the possible sensitivity of other contrasts to unmyelinated neuronal fibres, dMRI remains at present the most usually-applied MR modality for extracting information about the microstructural distribution of neuronal fibres.

Compared to dMRI of white matter, which is now becoming ever more routinely used (Horsfield and Jones, 2002; Sundgren et al., 2004), in vivo dMRI of cortex is more challenging. This is due to two main difficulties.

The first difficulty is in acquiring data of sufficient quality. Cortical dMRI is strongly affected by the artefacts mentioned in Section *Challenges of cortical MRI*. The relatively complex, almost isotropic orientational distribution of the neuronal fibres in cortex also means that a high diffusion weighting must be applied to probe the anisotropic component of this distribution, resulting in a diffusion-weighted signal with low SNR. Making scan time reasonable for in vivo subjects is also a challenge, requiring the use of highly accelerated pulse sequences with concomitant artefacts that then need to be corrected for (Ruthotto et al., 2012; Andersson and Sotiropoulos, 2016). Recent advances made possible by advanced acquisitions (Setsompop et al., 2018) and hardware (Setsompop et al., 2013), as well as advanced post-processing techniques such as adaptive denoising (Mohammadi et al., 2015) give hope for the future of laminar cortical analysis in vivo.

The second difficulty lies in interpreting the dMRI data (Alexander et al., 2018). Appropriate diffusion model assumptions have proven far harder to pin down in grey matter than in white matter, where it is accepted that the main source of diffusion anisotropy is the restriction and hindrance of water diffusion by myelinated axons. This is because the situation in cortex is much more complicated: myelinated axons (Leuze et al., 2017), unmyelinated axons (Nair et al., 2005), dendrites (Jespersen et al., 2007, 2012), and even neuronal cell bodies (Shemesh et al., 2015) provide barriers to diffusion and are thus potential sources of cortical diffusion contrast. Correlations between histological myelin

content and diffusion metrics suggest myelinated axons are still the main source of hindrance and restriction to diffusion in cortex (Leuze et al., 2014, 2017), but dendrites and unmyelinated axons contribute to the observed anisotropic diffusion (Nair et al., 2005; Jespersen et al., 2007, 2012; Zhang et al., 2012), though to a lesser extent due to the effects of exchange through the cell membrane (Yang et al., 2018) and the dendritic branching structure (Van Nguyen et al., 2015).

Tying these two difficulties together is the choice of acquisition scheme for cortical dMRI (Alexander et al., 2018). The optimal scheme will depend upon the model to be used (Alexander and Barker, 2005; Drobnyak et al., 2016; Nilsson et al., 2017), and must minimise sensitivity to artefacts (e.g. through minimising acquisition time to reduce sensitivity to motion). Recent studies have suggested that acquisition schemes appropriate for grey matter differ from those optimal for white matter (Chuhutin et al., 2017), and that classical diffusion acquisition schemes may be complemented by more advanced acquisition schemes (Novikov et al., 2014; Drobnyak et al., 2016; Shemesh et al., 2016; Ianuş et al., 2017).

Applications

Despite controversies regarding model choice, dMRI has been applied to attempt to quantify neuronal fibre-volume fractions and orientation distributions in vivo in human cortex (Morris et al., 2016). Splitting the populations of neuronal fibres into radial and tangential fibres on surfaces defined at different cortical depths (McNab et al., 2013; Kleinnijenhuis et al., 2015) further allows determination of how the ratio of forward/backward versus lateral connections varies throughout cortex, granting access to connectivity information complementary to that available using myelin-mapping methods.

Age-related changes in the cortex have also been investigated, with decreases in fibre orientation dispersion (Nazeri et al., 2015) and increases in a speculative metric of tissue heterogeneity (Rathi et al., 2014) showing macroscopic patterns reflecting age-related degeneration known from other methods of investigation. It has been speculated that these changes could be due to age-related changes in dendritic morphology (Nazeri et al., 2015).

Diffusion imaging has also been used to parcellate the cortex in vivo, as exemplified by Nagy et al. (2013), who utilised a feature extraction method to avoid making any assumptions about the source of anisotropic diffusion contrast. Calamante et al. (2018) have recently shown that model-based approaches could also allow for in vivo cortical parcellation.

In principle, cortical dMRI can also be used to study intracortical connectomics using tractography approaches, as is now routine in white matter studies (Behrens et al., 2014). Ex vivo investigations have shown intracortical tractography to be possible (Fig. 5; Leuze et al., 2014; Aggarwal et al., 2015), with Leuze et al. (2014) in particular using the technique to demonstrate preferential connections between primary and secondary visual cortex. However, the resolution and SNR available in vivo is at present insufficient for intracortical tractography.

As mentioned above, it has been suggested that PD and T_1 could be sensitive to neuronal fibres and not just myelin content (Gomez et al., 2017). More specifically, Gomez et al. (2017) combined PD and T_1 mapping to demonstrate that changes in regions of the developing child brain (localised using fMRI) are not purely down to myelination, but could be due to the proliferation of other cortical constituents such as dendrites.

Summary

Cortical dMRI allows the extraction of information about the cortical neuronal fibre distribution that cannot at present be extracted any other way in vivo. It can, for instance, allow disentanglement of intralaminar (tangential) and interlaminar (radial) connectivity in the cortex (McNab et al., 2013; Kleinnijenhuis et al., 2015), information that is very useful in studies of behaviour (Morris et al., 2016), and could be useful for cortical parcellation (Nagy et al., 2013). Unfortunately, limitations in terms of

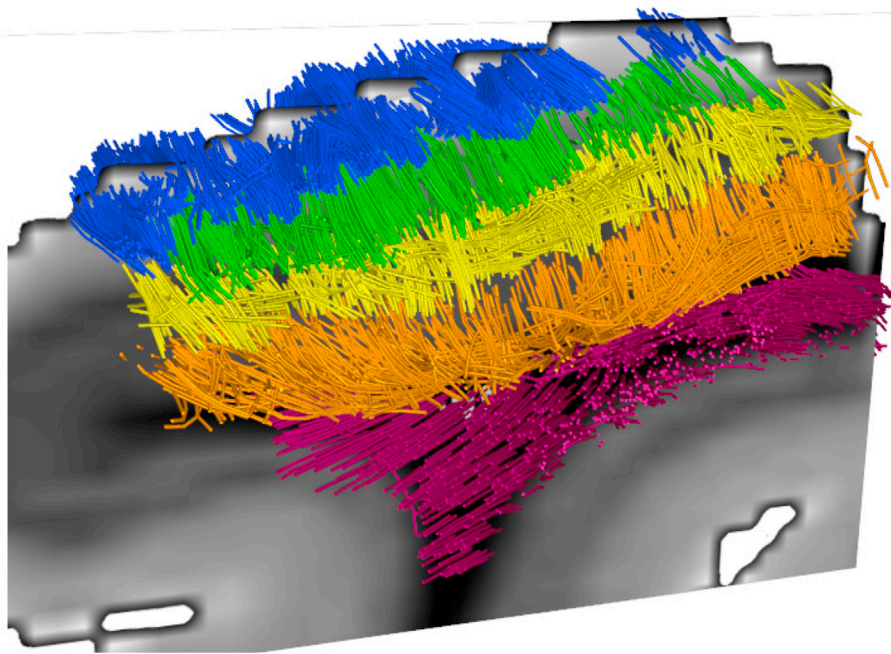


Fig. 5. Diffusion MRI has proven itself capable of extracting high resolution connectivity information *ex vivo*. Shown is the result of applying tractography algorithms to diffusion data from an *ex vivo* sample of human occipital cortex recorded at a resolution of $(0.242 \text{ mm})^3$ on a 9.4 T scanner. The cortex was split into four laminae for the purposes of building cortical profiles, and the tracts are labelled according to the lamina in which they are in: the superficial lamina is blue, the external lamina is green, the internal lamina is yellow, the deep lamina is orange, and the white matter is purple. Figure adapted from [Leuze et al. \(2014\)](#).

acquisition and modelling have so far limited the utility of cortical neuronal fibre mapping in *vivo*. Overcoming these limitations is the subject of active investigation, meaning cortical dMRI holds great promise for in *vivo* neuronal fibre mapping in the future.

Iron mapping: from glial cells to senile plaques

MRI techniques

Paramagnetic iron is an important contributor to MR contrast in the human cortex. The cortical paramagnetic iron-containing compounds described in Section [Cortical architecture: what we want to see!](#) affect MR contrast through several mechanisms at different length scales.

On the length scale of individual molecules, nanoscale molecular spin–spin interactions ([Abragam, 1961](#)) between water protons and the paramagnetic-iron core of ferritin contribute to iron-induced relaxation rates ([Gossuin et al., 2000, 2002, 2007; Hocq et al., 2015](#)). On the microscopic scale, cellular and sub-cellular distributions of iron induce local perturbations of the magnetic field, giving rise to enhanced R_2 and R_2^* relaxation through a variety of mechanisms ([Yablonskiy and Haacke, 1994; Kiselev and Novikov, 2002; Stüber et al., 2014; Yablonskiy and Sukstanskii, 2017](#)). On the mesoscopic scale, the intracortical variation of iron concentration is responsible for much of the pronounced cortical layer dependence of R_2^* ([Yao et al., 2009; Fukunaga et al., 2010; Deistung et al., 2013; Stüber et al., 2014; Duyn and Schenck, 2017](#)). The distribution of paramagnetic iron on the mesoscopic scale also perturbs the phase of the MR signal, which can be localised using QSM ([Fukunaga et al., 2010; Langkammer et al., 2012; Deistung et al., 2013; Acosta-Cabronero et al., 2016; Betts et al., 2016; Zhao et al., 2016](#)). Because different cortical layers and areas have different iron distributions ([Fukunaga et al., 2010](#)), iron mapping techniques making use of the above parameters can be used to map cortical architecture.

Different quantitative MR parameters have different sensitivities to paramagnetic iron. The sensitivities of R_1 and R_2^* to paramagnetic iron

were examined by [Stüber et al. \(2014\)](#) in *ex vivo* samples of human cortex at 7 T. From the results of [Stüber et al. \(2014\)](#), we estimate² that paramagnetic iron induced $\approx 20\%$ of their observed R_2^* . [Stüber et al. \(2014\)](#) also presented data showing³ that paramagnetic iron induced less than 10% of R_1 in human cortical samples at 7 T. It should be borne in mind that these numbers were obtained at 7 T in post mortem tissue samples, and so differences may be observed at different magnetic field strengths and in the *in vivo* case.

An important question arises: which mechanism dominates the iron-induced contribution to R_2^* ? Is it nanoscale molecular interactions, or the micro-/mesoscopic cellular iron distribution? The contributions of molecular interactions of water molecules with ferritin-bound iron to R_2 (and thus R_2^*) have been well studied ([Gossuin et al., 2000, 2002, 2007; Hocq et al., 2015](#)), but we estimate⁴ that these interactions only account for about 10% of the iron-induced contributions to cortical R_2^* at 7 T. The inhomogeneous iron distribution at the micro- and mesoscopic scale therefore potentially induces more than 90% of the intracortical iron-induced R_2^* value at 7 T.

Information about microscopic structures (e.g. glial cells and myelinated fibres) and mesoscopic structures (e.g. cortical layers) and their respective iron loads could thus potentially be extracted from quantitative MR maps.

Since myelinated fibres and the somata of oligodendrocytes, astrocytes, and microglia represent particularly iron-rich compartments in the cortex ([Fig. 1j](#)), we suggest that these are the main contributors to iron-induced R_2^* contrast. However, no generative models of iron-induced contrasts in cortex yet exist, thus extracting information about iron rich microstructures from MR parameters remains challenging. This is partly because only very limited quantitative information about the cellular

² Using the multilinear fit values reported in [Stüber et al. \(2014, Table 1\)](#), $\Delta R_2^* = 0.0526 [\text{Fe}] \text{ s}^{-1} \approx 14 \text{ s}^{-1}$ based on an intracortical iron concentration $[\text{Fe}] = 276 \mu\text{g/g dry mass}$ (an average value reported for primary motor/somatosensory cortex in [Stüber et al. \(2014\)](#)), as compared to a typical $R_2^* \approx 70 \text{ s}^{-1}$ (based on [Stüber et al. \(2014, Fig. 3\)](#)).

³ [Stüber et al. \(2014, Fig. 6\)](#) examined changes in R_1 resulting from chemically removing iron from the cortex. They reported $\Delta R_1 \approx 0.14 \text{ s}^{-1}$, relative to $R_1 \approx 1.54 \text{ s}^{-1}$ before iron removal.

⁴ Multiplying a typical intracortical iron concentration ($276 \mu\text{g/g dry mass}$ in human motor/somatosensory cortex ([Stüber et al., 2014](#))) with the R_2 relaxivity of ferritin-bound iron measured in solution (128 s^{-1} at an iron concentration of 100 mmol/dm^3 at 7 T from [Gossuin et al. \(2000, Fig. 1\)](#), which scales linearly to a tissue value of $0.0023 \text{ s}^{-1}(\mu\text{g/g dry mass})$) gives an $R_2 \approx 6.3 \text{ s}^{-1}$, as compared to a typical *ex vivo* cortical R_2^* of 70 s^{-1} ([Stüber et al., 2014](#)).

distribution of iron in the human cortex is available. Combination of advanced methods for iron quantification at the microscopic scale with qMRI of post mortem tissue and biophysical modelling could provide important insights in the future.

The phase of the MR signal is also sensitive to paramagnetic iron, providing the basis for MRI-based iron mapping methods using QSM (Schweser et al., 2011; Langkammer et al., 2010, 2012; Deistung et al., 2013; Acosta-Cabronero et al., 2016). Unfortunately, both paramagnetic iron (positive susceptibility) and diamagnetic myelin (negative susceptibility) contribute to QSM contrast, causing partial cancellation in the cortex (Schweser et al., 2011), making the interpretation of QSM metrics challenging, especially in light of the interrelationship of iron and myelin concentrations observed in some cortical areas (Section [Cortical architecture: what we want to see!](#)).

Attempts to disentangle iron and myelin contributions to MR contrast through empirical linear modelling and the collection of multiple complementary quantitative images (Stüber et al., 2014; Marques et al., 2017) were discussed in Section [Myelin mapping: myeloarchitecture in vivo](#).

It is important to bear in mind that capillaries and vessels also contribute to R_2^* and QSM contrast in the cortex, because the deoxygenated haemoglobin contained within is paramagnetic. The dynamic portion of this contribution is the basis of blood oxygenation level-dependent (BOLD) fMRI (Uludağ et al., 2005), and will not be discussed further here. Investigation of the static contribution by Zhao et al. (2016) found that it accounted for about 10% of cortical R_2^* at 3 T, and that this contribution was age dependent. As of yet, however, there has been no investigation regarding the specific laminar dependence of this contribution, and the effect is likely to be B_0 -dependent. Evaluation of the vascular contribution to MRI-based iron markers would be an important step in increasing the specificity of these markers to specific sources of iron.

Applications

The colocalisation of cortical iron and myelin observed in some cortical areas (Fukunaga et al., 2010) implies that R_2^* could be a sensitive probe of cortical myeloarchitecture, because both paramagnetic iron and myelin increase R_2^* . In line with this, an investigation using ex vivo human brain tissue found that R_2^* provided the highest contrast between myeloarchitectonic areas, outperforming R_1 (Fukunaga et al., 2010). However, in contrast, R_1 -based cortical parcellation has been found to outperform R_2^* -based parcellation in vivo (Haast et al., 2016). This relative lack of robustness in vivo is potentially due to artefacts resulting from vasculature containing deoxygenated haemoglobin (Ulrich and Yablonskiy, 2016), the orientation-dependence of the contribution from myelinated fibres, susceptibility artefacts arising from the sharp boundaries between different tissues (Cohen-Adad et al., 2012; Cohen-Adad, 2014; Tardif et al., 2015; Marques et al., 2017), and the relatively high sensitivity of R_2^* to motion (Magerkurth et al., 2011) and physiological artefacts (Versluis et al., 2010).

Investigation of age-related cortical iron accumulation in health and disease is another important potential application of intracortical in vivo iron mapping: the possibility of using the accumulation of brain iron as a biomarker for neurodegeneration promises high diagnostic relevance. As mentioned in Section [Cortical architecture: what we want to see!](#), histological investigations have shown that the ageing brain accumulates iron at different rates in different cortical areas (Hallgren and Sourander, 1958). These histological findings have recently been reproduced with MRI in vivo (Fig. 6), using MR signal phase (Buijs et al., 2017), R_2^* (Callaghan et al., 2014; Betts et al., 2016), and QSM (Acosta-Cabronero et al., 2016) as markers for iron content. However, differences between results obtained using R_2^* and QSM imaging (Betts et al., 2016) suggest either that both iron accumulation and demyelination contribute to ageing-related changes, or that the iron distribution at the microscopic scale is more complex than assumed.

Neuroscientific investigations have also attempted to correlate MR derived cortical iron content in adult brains with behavioural and cognitive metrics. Such investigations have found increased iron content to be correlated with certain of these behavioural and cognitive metrics (Allen et al., 2017a; b).

Iron-induced contrast in the cortex could also provide unique early-onset markers for several neurodegenerative diseases (Bartzokis et al., 2004; Quintana et al., 2006; Kwan et al., 2012; Meadowcroft et al., 2015; Costagli et al., 2016; Zhao et al., 2017). For instance, the cortical micro- and mesoscopic senile plaques and neurofibrillary tangles associated with Alzheimer's disease contain a relatively high concentration of iron (Morawski et al., 2005; van Duijn et al., 2017), and therefore induce detectable QSM and R_2^* contrast (Benveniste et al., 1999; Jack et al., 2005; Meadowcroft et al., 2015; O'Callaghan et al., 2017) which may be detectable in vivo (Zhao et al., 2017). As another example, in ALS, iron accumulation in the deep cortical layers of motor cortex is detectable with MRI (Kwan et al., 2012; Costagli et al., 2016). It has been suggested that this biomarker could be driven by activated microglia (Kwan et al., 2012).

Summary

Mapping of MRI-based iron markers in the cortex is increasingly being applied to parcellate the brain and to find correlates of functions of neuroscientific interest. It is also being investigated as a tool to study the neurobiology of ageing and clinical neurodegenerative diseases. Most of the studies used R_2^* or QSM as iron markers, with a few studies combining multiple complementary MR images. Unfortunately, it remains unknown which of the iron-containing cortical constituents described in Section [Cortical architecture: what we want to see!](#) contribute most to the MR-visible iron, as quantitative knowledge about the distribution of iron on the microscopic scale is limited. Advanced quantitative histological methods for iron mapping will be needed to overcome this knowledge gap (Morawski et al., 2005; Stüber et al., 2014; Hare et al., 2015).

Other biological substrates and MR methods

The discussion of MRI methods and contrast above has not covered all of the characteristic microstructural features of the cortex described in Section [Cortical architecture: what we want to see!](#). Foremost of these is cytoarchitecture. Outside of highly specialised acquisitions only possible ex vivo (Eickhoff et al., 2005; Wei et al., 2016), the direct effect of cell bodies on the MRI signal is at best non-specific (Shemesh et al., 2015), and normally negligible. It has, however, been suggested that neuronal cell-body packing density could affect T_2^* (Zhao et al., 2016), T_1 and PD (Gomez et al., 2017) measurements.

The relationship between cortical myelin density and cytoarchitecture could in principle be used to indirectly provide cytoarchitectonic maps in vivo (Turner and De Haan, 2017). A concrete example is provided by the forward model of Dinse et al. (2015): neuronal cell body distributions from von Economo and Koskinas (1925) were used to generate myeloarchitectonic profiles (following Hellwig (1993)), which were in turn used to simulate T_1 cortical profiles to compare with experimental in vivo data. However, the relative sparsity of myeloarchitectonic information on the mesoscopic scale, especially in the upper layers of cortex, means that such models are probably not invertible and that they could not, in the absence of further information, be used to infer cytoarchitecture from T_1 profiles.

Magnetic resonance spectroscopy (MRS), a method for probing nuclei besides water protons with MR techniques, could allow us to explore structures of the brain with greater specificity (Palombo et al., 2018). Many MRS techniques have been developed (Ross and Bluml, 2001), and their potentially greater specificity arises from different molecules, e.g. neurotransmitters, being localised in different biological compartments (Najac et al., 2016; Palombo et al., 2016, this special issue).

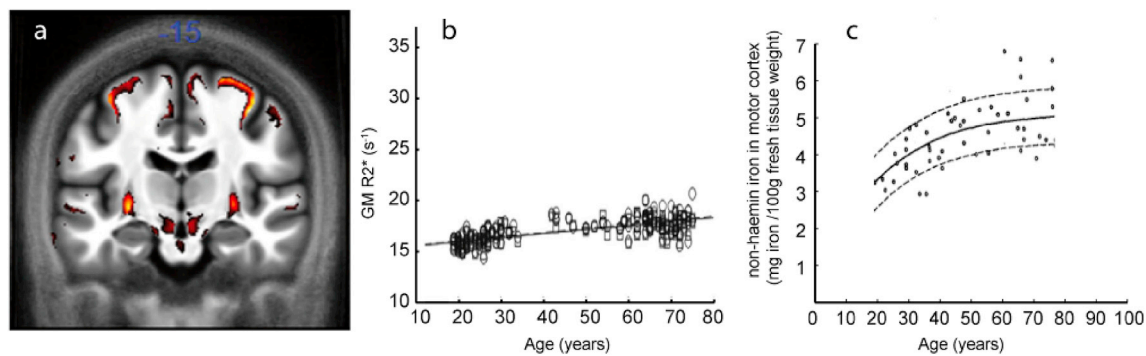


Fig. 6. Area-specific iron accumulation in ageing cortex as studied by MRI in vivo supports earlier post mortem histological findings. (a) Map of brain areas that showed significant increase in R_2^* in line with an increased iron concentration with age (reproduced from Callaghan et al. (2014)). (b) Age dependence of iron marker R_2^* in supplementary motor cortex (reproduced from Callaghan et al. (2014)). (c) Age dependence of iron content in motor cortex as studied by histology (replotted from Hallgren and Sourander (1958)).

Unfortunately, this gain in specificity is coupled to an extreme increase in acquisition times, and low SNR due to the much lower concentrations of such molecules as compared to water in the human brain. This results in a strict voxel size limitation, and such techniques are usually limited to recording data from a very small number of voxels, typically just one. Techniques such as chemical exchange saturation transfer (CEST) can help to mitigate the SNR problem (van Zijl and Yadav, 2011; Jin et al., 2013; Vinogradov et al., 2013; Sled, 2018), but are limited to a small range of molecules and face challenges in terms of molecular specificity. Nevertheless, studies have demonstrated that useful information can be gleaned from MRS methods in human and rodent cortex (Mougin et al., 2013; Palombo et al., 2016; Henning, 2017; Palombo et al., 2018). Advances in parallel imaging and pulse sequence design could make such acquisitions more feasible for probing the brain in vivo, meaning they could provide an interesting opportunity for validating other higher resolution methods and models (Grossman et al., 2015; Palombo et al., 2018).

Another complementary MR method for collecting information about the brain is magnetic resonance elastography (MRE), wherein the brain is subjected to some form of mechanical oscillation during the acquisition of MR images. The effect of the oscillations on the phase of the MR signal can be used to infer elastographic properties of brain tissue (Muthupillai et al., 1995; Hiscox et al., 2016). MRE has shown promise for the development of biomarkers for the study of ageing and pathology, however most studies limit themselves to extracting whole brain parameters (Hiscox et al., 2016; Johnson and Telzer, 2017). Localisation of elastographic properties to the cortex has been reported (McGarry et al., 2013; Braun et al., 2014; Hiscox et al., 2016), but further work is needed to increase robustness and decrease susceptibility to partial volume effects (Johnson and Telzer, 2017).

Conclusions and outlook

We now draw a few general conclusions, followed by an outlook to future developments.

Our first conclusion is that hMRI is gradually becoming a reality, and in some areas already providing insights that would not be possible with classical histology. In vivo mapping of myelin content using relaxometry has proved very successful (Section [Myelin mapping: myeloarchitecture in vivo](#)); an example is the parcellation of Glasser et al. (2016), derived by combining a myelin marker with fMRI data, which would neither have been as feasible nor as useful had it been defined based upon several hundred cadaver brains. Glasser et al. (2016)'s parcellation also exemplifies an important facet of hMRI: the ability to correlate structure and function in the cortex of the same brain. Similarly, in vivo iron mapping (Section [Iron mapping: from glial cells to senile plaques](#)) has allowed extension of known ex vivo results regarding changes in iron load with

age (Hallgren and Sourander, 1958) into much larger cohorts (Callaghan et al., 2014), and will enable longitudinal studies of the same brain. In vivo techniques for probing the microstructure of neuronal fibres, the third biological substrate we examined in detail (Section [Neuronal fibre mapping: intracortical connectomics](#)), are not yet as developed as myelin and iron mapping techniques, but this area of investigation shows great promise.

Secondly, we conclude that specificity to microstructural features requires combining images with complementary sensitivity to the biological substrate of interest (Cercignani and Bouyagoub, 2018), with a tendency towards the use of qMRI. The need for complementary images is well exemplified when examining the use of “myelin markers”. While many MR images show contrast suggestive of being driven by changes in myelin content (Section [Myelin mapping: myeloarchitecture in vivo](#)), studies that have tried to disentangle the myelin contribution to contrast from other contributions (e.g. iron (Stüber et al., 2014; Marques et al., 2017) and neuronal fibres (Gomez et al., 2017)) have demonstrated that the concept of a myelin marker is an oversimplification. The quest for specific markers also explains the large number of studies utilising quantitative images: quantitative images are more acquisition-scheme independent (Weiskopf et al., 2013; Stikov et al., 2015), and so can give rise to more generalisable conclusions.

While substantial progress has been made, it is clear that there is still a way to go until hMRI unleashes its full potential. The main problem remains specificity: what is the micro- or mesostructural origin of an observed intra- or inter-subject MRI-signal difference? Based on the above, we believe that the way forward involves further methodological developments incorporating multiple MR modalities probing a greater range of scales, coupled with appropriate models to integrate this data. We will cover each of these topics in turn.

Different MRI methods are sensitive to different aspects of cortical microstructure, and have different length scale sensitivity and restrictions with regard to resolution. In order to investigate the rich amount of information available in the neocortical microstructure (Section [Cortical architecture: what we want to see!](#)), we must thus record multiple complementary quantitative images at the meso- or macroscopic scales (Cercignani and Bouyagoub, 2018). In particular, combination of the more specific information from the methods described in Section [Other biological substrates and MR methods](#) with more sensitive methods (e.g. R_1 ; see Section [Myelin mapping: myeloarchitecture in vivo](#)) could allow more specific inferences to be made than is possible with either alone.

The resolution of the acquired data must also be as high as possible, with mesoscopic-scale voxel sizes preferable; many of the reviewed articles recorded at least one anatomical image at the mesoscopic scale. The reviewed articles show a clear trend to higher B_0 (7 T and upwards), with the improved SNR thus generated allowing smaller voxel sizes. Access to

ultra high field systems is growing, and new specialised hardware including bespoke gradient systems (Setsompop et al., 2013), prospective motion correction systems (Callaghan et al., 2015b; Stucht et al., 2015), and magnetic field camera systems (Wilm et al., 2015; Dietrich et al., 2016) will push the boundaries of currently available resolutions by reducing the prominence of artefacts and increasing SNR. Advanced post-processing techniques such as super-resolution imaging (Ruthotto et al., 2014; Setsompop et al., 2018) and adaptive denoising (Tabelow et al., 2015; Veraart et al., 2016) may be required to access high spatial resolutions, especially in the case of dMRI.

Regarding appropriate models, multiple quantitative images can be combined to give greater specificity, but only if a sufficiently capable model is used to integrate the data. An example is provided by attempts to extract iron and myelin maps through a combination of R_1 , R_2^* , and QSM, as described in Section *Myelin mapping: myeloarchitecture in vivo*. While a linear model was sufficient to extract iron and myelin maps ex vivo (Stüber et al., 2014), the in vivo case was found to be more complex (Marques et al., 2017), with different model assumptions perhaps needed for in vivo application. Looking to the future, generalised models incorporating more quantitative images will allow greater specificity in inferences. Such models would also facilitate the design of optimal acquisitions (Alexander and Barker, 2005; Cercignani and Alexander, 2006; Drobniak et al., 2016; Nilsson et al., 2017), and the inclusion of pathology (Zhao et al., 2017).

In particular, mapping iron microstructure requires development of generative models of iron-induced contrast. Systematic quantitative mapping of iron across whole post mortem brains at the macro-, meso- and microscopic scales is required to inform such models, and is currently under development in several labs (including our own; Morawski et al., 2018).

Similar considerations apply to dMRI, where biophysical models in the cortex (see e.g. Jespersen et al. (2007, 2012)) would benefit from being informed by advanced 3d histological methods (Morawski et al., 2018).

Lastly, we briefly mention the important topic of validation. Ex vivo validation is important for validating models, but can only with care be used as a gold standard, because:

- structural changes can arise from the fixation/decay process (Schmierer et al., 2008, 2010; Shepherd et al., 2009; Birkl et al., 2016, 2018);
- comparisons to MRI are normally complicated by a rarity of quantitative true-3d histology techniques (Hilgetag and Amunts, 2016; Morawski et al., 2018);
- the MRI acquisition regime may be vastly different to that possible for in vivo human subjects; and
- the differences between individual brains can be large (Ono et al., 1990; Rademacher, 2002).

Most of these problems are exacerbated in the (frequent) case that non-human tissue is used, adding the complication of inter-species comparison. However, modern histological techniques are pushing the boundaries of what is achievable and allowing the extraction of ever more quantitative and ever more reliable results (Chung and Deisseroth, 2013; Stüber et al., 2014; Amunts and Zilles, 2015; Hare et al., 2015; Leuze et al., 2017; Morawski et al., 2018).

In vivo human cortical MRI is sensitive to, and therefore allows in vivo investigation of, many of the macroscopic, mesoscopic and microscopic aspects of cortical architecture described in Section *Cortical architecture: what we want to see!* and presented in Fig. 1. On the macroscopic scale, cortical parcellation into functional and structural areas using 3 T of large groups of subjects represents a major achievement (Fig. 1c). Parcellation of primary visual, sensory-motor and auditory areas is feasible on the single-subject level by using ultra-high field strength 7 T MRI, mostly based on high myelin content of primary areas (Fig. 4). On the mesoscopic scale, identification of cortical layers using

structural MRI (Fig. 1d and e) becomes feasible at ultra-high field strengths in vivo, and could be used to identify higher cortical areas (Trampel et al., 2018). Combination of layer-specific anatomical MRI with recent achievements in layer-specific fMRI techniques (Huber et al., 2017a; b; Dumoulin et al., 2018; Lawrence et al., 2017) holds particular promise. Moreover, mesoscopic cortical organisation units such as columns and stripes (Fig. 1f) might be detectable throughout the brain using structural MRI, as has recently been demonstrated in visual cortex (Dumoulin et al., 2017). On the microscopic scale, the use of dMRI to differentiate tangential and radial intracortical fibre populations, and thus intralaminar versus forward/backward connection strength, holds promise for future work. Finally, total iron content in the cortex (Fig. 1j) could be estimated using combination of several contrasts, as has already been demonstrated ex vivo (Stüber et al., 2014). The development of theoretical models and application of advanced iron quantification methods shows potential for the extraction of more specific information regarding the microstructural distribution of iron-rich cells and fibres.

With practical applications now beginning to be realised, researchers in the field of hMRI will continue to push for greater specificity and greater sensitivity. We anticipate that derived techniques will eventually take their place in the routine corpus of clinical and neuroscientific investigations.

Acknowledgements

NW and LJE were supported by the European Research Council under the European Union's Seventh Framework Programme (FP7/2007–2013) / ERC grant agreement No 616905. NW was supported by the NISCI project funded by the European Union's Horizon 2020 research and innovation programme under the grant agreement No. 681094 and the Swiss State Secretariat for Education, Research and Innovation (SERI) under contract number 15.0137; and received funding from the BRAINTRAIN European research network (Collaborative Project) supported by the European Commission under the Health Cooperation Work Programme of the 7th Framework Programme (Grant agreement No. 602186). NW and SM received funding from the BMBF (01EW1711A and B) in the framework of ERA-NET NEURON. SM received funding from the European Union's Horizon 2020 research and innovation programme under the Marie Skłodowska-Curie grant agreement No 658589 and was supported by the Deutsche Forschungsgemeinschaft, Grant Number: MO 2397/4-1. We thank Stefan Geyer for helpful comments on the manuscript.

References

- Abraham, A., 1961. *The Principles of Nuclear Magnetism*. International Series of Monographs on Physics. OUP, Oxford.
- Absinta, M., Ha, S.K., Nair, G., Sati, P., Luciano, N.J., Palisoc, M., Louveau, A., Zaghoul, K.A., Pittaluga, S., Kipnis, J., Reich, D.S., 2017. Human and nonhuman primate meninges harbor lymphatic vessels that can be visualized noninvasively by MRI. *eLife* 6, e29738. <https://doi.org/10.7554/eLife.29738>.
- Acosta-Cabrero, J., Betts, M.J., Cardenas-Blanco, A., Yang, S., Nestor, P.J., 2016. In vivo MRI mapping of brain iron deposition across the adult lifespan. *J. Neurosci.* 36, 364–374. <https://doi.org/10.1523/JNEUROSCI.1907-15.2016>.
- Adams, D.L., Piserchia, V., Economides, J.R., Horton, J.C., 2015. Vascular supply of the cerebral cortex is specialized for cell layers but not columns. *Cereb. Cortex* 25, 3673–3681. <https://doi.org/10.1093/cercor/bhu221>.
- Aggarwal, M., Nauen, D.W., Troncoso, J.C., Mori, S., 2015. Probing region-specific microstructure of human cortical areas using high angular and spatial resolution diffusion MRI. *NeuroImage* 105, 198–207. <https://doi.org/10.1016/j.neuroimage.2014.10.053>.
- Alexander, D.C., Barker, G.J., 2005. Optimal imaging parameters for fiber-orientation estimation in diffusion MRI. *NeuroImage* 27, 357–367. <https://doi.org/10.1016/j.neuroimage.2005.04.008>.
- Alexander, D.C., Dyrby, T.B., Nilsson, M., Zhang, H., 2018. Imaging brain microstructure with diffusion MRI: practicality and applications. *NMR Biomed.* <https://doi.org/10.1002/nbm.3841> (in press).
- Allen, M., Frank, D., Glen, J.C., Fardo, F., Callaghan, M.F., Rees, G., 2017a. Insula and somatosensory cortical myelination and iron markers underlie individual differences in empathy. *Sci. Rep.* 7, srep43316 <https://doi.org/10.1038/srep43316>.
- Allen, M., Glen, J.C., Müllensiefen, D., Schwarzkopf, D.S., Fardo, F., Frank, D., Callaghan, M.F., Rees, G., 2017b. Metacognitive ability correlates with hippocampal

- and prefrontal microstructure. *NeuroImage* 149, 415–423. <https://doi.org/10.1016/j.neuroimage.2017.02.008>.
- Amunts, K., Zilles, K., 2015. Architectonic mapping of the human brain beyond Brodmann. *Neuron* 88, 1086–1107. <https://doi.org/10.1016/j.neuron.2015.12.001>.
- Andersson, J.L.R., Sotiropoulos, S.N., 2016. An integrated approach to correction for off-resonance effects and subject movement in diffusion MR imaging. *NeuroImage* 125, 1063–1078. <https://doi.org/10.1016/j.neuroimage.2015.10.019>.
- Annese, J., Pitiot, A., Dinov, I.D., Toga, A.W., 2004. A myelo-architectonic method for the structural classification of cortical areas. *NeuroImage* 21, 15–26. <https://doi.org/10.1016/j.neuroimage.2003.08.024>.
- Barres, B.A., Freeman, M.R., Stevens, B. (Eds.), 2015. *Glia*. Cold Spring Harbor Laboratory Press, New York.
- Bartzokis, G., Tishler, T.A., Shin, I.S., Lu, P.H., Cummings, J.L., 2004. Brain ferritin iron as a risk factor for age at onset in neurodegenerative diseases. *Ann. N. Y. Acad. Sci.* 1012, 224–236. <https://doi.org/10.1196/annals.1306.019>.
- Basser, P.J., Özarslan, E., 2011. Anisotropic diffusion: from the apparent diffusion coefficient to the apparent diffusion tensor. in: Jones (2011). Chapter 6, pp. 79–91.
- Bazin, P.L., Weiss, M., Dinse, J., Schäfer, A., Trampel, R., Turner, R., 2014. A computational framework for ultra-high resolution cortical segmentation at 7 Tesla. *NeuroImage* 93, 201–209. <https://doi.org/10.1016/j.neuroimage.2013.03.077>.
- Beaulieu, C., 2011. What makes diffusion anisotropic in the nervous system? in: Jones (2011). Chapter 7, pp. 92–109.
- Behrens, T.E.J., Sotiropoulos, S.N., Jbabdi, S., 2014. MR diffusion tractography. In: Johansen-Berg, H., Behrens, T.E.J. (Eds.), *Diffusion MRI: from Quantitative Measurement to In-vivo Neuroanatomy*, second ed. Academic Press, London. <https://doi.org/10.1016/B978-0-12-396460-1.00019-6>. chapter 19, pp. 429–451.
- Benveniste, H., Einstein, G., Kim, K.R., Hulette, C., Johnson, G.A., 1999. Detection of neuritic plaques in Alzheimer's disease by magnetic resonance microscopy. *Proc. Natl. Acad. Sci.* 96, 14079–14084. <https://doi.org/10.1073/pnas.96.24.14079>.
- Berman, S., West, K.L., Does, M.D., Yeatman, J.D., Mezer, A.A., 2018. Evaluating g-ratio weighted changes in the corpus callosum as a function of age and sex. *NeuroImage* 182, 304–313.
- Betts, M.J., Acosta-Cabrero, J., Cardenas-Blanco, A., Nestor, P.J., Düzel, E., 2016. High-resolution characterisation of the aging brain using simultaneous quantitative susceptibility mapping (QSM) and R_2^* measurements at 7T. *NeuroImage* 138, 43–63. <https://doi.org/10.1016/j.neuroimage.2016.05.024>.
- Beul, S.F., Barbas, H., Hilgetag, C.C., 2017. A predictive structural model of the primate connectome. *Sci. Rep.* 7, srep43176 <https://doi.org/10.1038/srep43176>.
- Birkel, C., Langkammer, C., Golob-Schwarzl, N., Leoni, M., Haybaeck, J., Goessler, W., Fazekas, F., Ropele, S., 2016. Effects of formalin fixation and temperature on MR relaxation times in the human brain. *NMR Biomed.* 29, 458–465. <https://doi.org/10.1002/nbm.3477>.
- Birkel, C., Soellradl, M., Toeglhofer, A.M., Krassnig, S., Leoni, M., Pirpamer, L., Vorauer, T., Krenn, H., Haybaeck, J., Fazekas, F., Ropele, S., Langkammer, C., 2018. Effects of concentration and vendor specific composition of formalin on postmortem mri of the human brain. *Magn. Reson. Med.* 79, 1111–1115. <https://doi.org/10.1002/mrm.26699>.
- Blaimer, M., Breuer, F., Mueller, M., Heidemann, R.M., Griswold, M.A., Jakob, P.M., 2004. SMASH, SENSE, PILS, GRAPPA: how to choose the optimal method. *Top. Magn. Reson. Imag.* 15, 223–236. <https://doi.org/10.1097/01.mrm.0000136558.09801.dd>.
- Braak, H., 1980. Architectonics of the Human Telencephalic Cortex. Number 4 in *Studies of Brain Function*. Springer, Berlin.
- Braitenberg, V., 1962. A note on myeloarchitectonics. *J. Comp. Neurol.* 118, 141–156. <https://doi.org/10.1002/cne.901180202>.
- Braitenberg, V., Schüz, A., 1998c. Density of axons. In: Braitenberg and Schüz (1998b). Chapter 7, pp. 39–42. https://doi.org/10.1007/978-3-662-03733-1_7.
- Braitenberg, V., Schüz, A., 1998a. Comparative aspects: statistical measures in larger brains. in: Braitenberg and Schüz (1998b), Chapter 34, pp. 189–192. https://doi.org/10.1007/978-3-662-03733-1_34.
- Braitenberg, V., Schüz, A., 1998b. *Cortex: Statistics and Geometry of Neuronal Connectivity*. Springer, Berlin, Heidelberg.
- Braun, J., Guo, J., Lützkendorf, R., Stadler, J., Papazoglou, S., Hirsch, S., Sack, I., Bernarding, J., 2014. High-resolution mechanical imaging of the human brain by three-dimensional multifrequency magnetic resonance elastography at 7T. *NeuroImage* 90, 308–314. <https://doi.org/10.1016/j.neuroimage.2013.12.032>.
- Bridge, H., Clare, S., 2006. High-resolution MRI: in vivo histology? *Phil. Trans. Roy. Soc. B Biol. Sci.* 361, 137–146. <https://doi.org/10.1098/rstb.2005.1777>.
- Brodmann, K., 1909. *Vergleichende Lokalisationslehre der Großhirnrinde*. Barth, Leipzig.
- Buijs, M., Doan, N.T., van Rooden, S., Versluis, M.J., van Lew, B., Milles, J., van der Grond, J., van Buchem, M.A., 2017. In vivo assessment of iron content of the cerebral cortex in healthy aging using 7-Tesla T_2^* -weighted phase imaging. *Neurobiol. Aging* 53, 20–26. <https://doi.org/10.1016/j.neurobiolaging.2016.09.005>.
- Bulte, J.W.M., van Zijl, P.C.M., Mori, S., 2002. Magnetic resonance microscopy and histology of the CNS. *Trends Biotechnol.* 20, S24–S28. [https://doi.org/10.1016/S0167-7799\(02\)00202-4](https://doi.org/10.1016/S0167-7799(02)00202-4).
- Calamante, F., Jeurissen, B., Smith, R.E., Tournier, J.D., Connelly, A., 2018. The role of whole-brain diffusion MRI as a tool for studying human in vivo cortical segregation based on a measure of neurite density. *Magn. Reson. Med.* 78, 2738–2744. <https://doi.org/10.1002/mrm.26917>.
- Callaghan, P.T., 1993. *Principles of Nuclear Magnetic Resonance Microscopy*. Oxford science publications, Clarendon Press, Oxford.
- Callaghan, M.F., Freund, P., Draganski, B., Anderson, E., Cappelletti, M., Chowdhury, R., Diedrichsen, J., FitzGerald, T.H.B., Smittenaar, P., Helms, G., Lutti, A., Weiskopf, N., 2014. Widespread age-related differences in the human brain microstructure revealed by quantitative magnetic resonance imaging. *Neurobiol. Aging* 35, 1862–1872. <https://doi.org/10.1016/j.neurobiolaging.2014.02.008>.
- Callaghan, M.F., Helms, G., Lutti, A., Mohammadi, S., Weiskopf, N., 2015a. A general linear relaxometry model of R_1 using imaging data: general linear relaxometry model of R_1 . *Magn. Reson. Med.* 73, 1309–1314. <https://doi.org/10.1002/mrm.25210>.
- Callaghan, M.F., Josephs, O., Herbst, M., Zaitsev, M., Todd, N., Weiskopf, N., 2015b. An evaluation of prospective motion correction (PMC) for high resolution quantitative MRI. *Front. Neurosci.* 9 <https://doi.org/10.3389/fnins.2015.00097>.
- Callaghan, M.F., Mohammadi, S., Weiskopf, N., 2016. Synthetic quantitative MRI through relaxometry modelling. *NMR Biomed.* 29, 1729–1738. <https://doi.org/10.1002/nbm.3658>.
- Campbell, J.S.W., Leppert, I.R., Narayanan, S., Boudreau, M., Duval, T., Cohen-Adad, J., Pike, G.B., Stikov, N., 2018. Promise and pitfalls of g-ratio estimation with MRI. *NeuroImage* 182, 80–96.
- Cercignani, M., Alexander, D.C., 2006. Optimal acquisition schemes for in vivo quantitative magnetization transfer MRI. *Magn. Reson. Med.* 56, 803–810. <https://doi.org/10.1002/mrm.21003>.
- Cercignani, M., Bouyagoub, S., 2018. Brain microstructure by multimodal MRI: greater than the sum of its parts? *NeuroImage* 182, 117–127.
- Chen, W.C., Foxley, S., Miller, K.L., 2013. Detecting microstructural properties of white matter based on compartmentalization of magnetic susceptibility. *NeuroImage* 70, 1–9. <https://doi.org/10.1016/j.neuroimage.2012.12.032>.
- Chuhutin, A., Hansen, B., Jespersen, S.N., 2017. Precision and accuracy of diffusion kurtosis estimation and the influence of b-value selection. *NMR Biomed.* 30, e3777 <https://doi.org/10.1002/nbm.3777>.
- Chung, K., Deisseroth, K., 2013. CLARITY for mapping the nervous system. *Nat. Meth.* 10, 508–513. <https://doi.org/10.1038/nmeth.2481>.
- Cohen-Adad, J., 2014. What can we learn from T_2^* maps of the cortex? *NeuroImage* 93 (Pt 2), 189–200. <https://doi.org/10.1016/j.neuroimage.2013.01.023>.
- Cohen-Adad, J., Polimeni, J.R., Helmer, K.G., Benner, T., McNab, J.A., Wald, L.L., Rosen, B.R., Mainero, C., 2012. T_2^* mapping and B_0 orientation-dependence at 7 T reveal cyto- and myeloarchitecture organization of the human cortex. *NeuroImage* 60, 1006–1014. <https://doi.org/10.1016/j.neuroimage.2012.01.053>.
- Connor, J.R., Menzies, S.L., 1996. Relationship of iron to oligodendrocytes and myelination. *Glia* 17, 83–93. [https://doi.org/10.1002/\(SICI\)1098-1136\(199606\)17:2<83::AID-GLIA1>3.0.CO;2-7](https://doi.org/10.1002/(SICI)1098-1136(199606)17:2<83::AID-GLIA1>3.0.CO;2-7).
- Connor, J.R., Menzies, S.L., St Martin, S.M., Mufson, E.J., 1990. Cellular distribution of transferrin, ferritin, and iron in normal and aged human brains. *J. Neurosci. Res.* 27, 595–611. <https://doi.org/10.1002/jnr.490270421>.
- Costagli, M., Donatelli, G., Biagi, L., Caldarazzo Ienco, E., Siciliano, G., Tosetti, M., Cosottini, M., 2016. Magnetic susceptibility in the deep layers of the primary motor cortex in amyotrophic lateral sclerosis. *NeuroImage. Clin.* 12, 965–969. <https://doi.org/10.1016/j.nicl.2016.04.011>.
- D'Arceuil, H., de Crespigny, A., 2011. Diffusion imaging in gray matter. in: Jones (2011). Chapter 39, pp. 647–660.
- De Biase, L.M., Schuebel, K.E., Fuschel, Z.H., Jair, K., Hawes, I.A., Cimbri, R., Zhang, H.Y., Liu, Q.R., Shen, H., Xi, Z.X., Goldman, D., Bonci, A., 2017. Local cues establish and maintain region-specific phenotypes of basal ganglia microglia. *Neuron* 95. <https://doi.org/10.1016/j.neuron.2017.06.020>, 341.e6–356.e6.
- De Martino, F., Moerel, M., Xu, J., van de Moortele, P.F., Ugurbil, K., Goebel, R., Yacoub, E., Formisano, E., 2015. High-resolution mapping of myeloarchitecture in vivo: localization of auditory areas in the human brain. *Cereb. Cortex* 25, 3394–3405. <https://doi.org/10.1093/cercor/bhu150>.
- Deichmann, R., Good, C.D., Josephs, O., Ashburner, J., Turner, R., 2000. Optimization of 3-D MP-RAGE sequences for structural brain imaging. *NeuroImage* 12, 112–127. <https://doi.org/10.1006/nimg.2000.0601>.
- Deistung, A., Schäfer, A., Schweser, F., Biedermann, U., Turner, R., Reichenbach, J.R., 2013. Toward in vivo histology: a comparison of quantitative susceptibility mapping (QSM) with magnitude-, phase-, and R_2^* -imaging at ultra-high magnetic field strength. *NeuroImage* 65, 299–314. <https://doi.org/10.1016/j.neuroimage.2012.09.055>.
- Deistung, A., Schweser, F., Reichenbach, J.R., 2017. Overview of quantitative susceptibility mapping. *NMR Biomed.* 30, e3569. <https://doi.org/10.1002/nbm.3569>.
- Dick, F., Tierney, A.T., Lutti, A., Josephs, O., Sereno, M.I., Weiskopf, N., 2012. In vivo functional and myeloarchitectonic mapping of human primary auditory areas. *J. Neurosci.* 32, 16095–16105. <https://doi.org/10.1523/JNEUROSCI.1712-12.2012>.
- Dietrich, B.E., Brunner, D.O., Wilm, B.J., Barmet, C., Gross, S., Kasper, L., Haeberlin, M., Schmid, T., Vannest, S.J., Pruessmann, K.P., 2016. A field camera for MR sequence monitoring and system analysis. *Magn. Reson. Med.* 75, 1831–1840. <https://doi.org/10.1002/mrm.25770>.
- Ding, S.L., Royall, J.J., Sunkin, S.M., Ng, L., Facer, B.A.C., Lesnar, P., Guillozet-Bongaarts, A., McMurray, B., Szafer, A., Dolbeare, T.A., Stevens, A., Tirrell, L., Benner, T., Caldejon, S., Dalley, R.A., Dee, N., Lau, C., Nyhus, J., Reding, M., Riley, Z.L., Sandman, D., Shen, E., van der Kouwe, A., Varjabedian, A., Wright, M., Zöllei, L., Dang, C., Knowles, J.A., Koch, C., Phillips, J.W., Sestan, N., Wahnoutka, P., Zielke, H.R., Hohmann, J.G., Jones, A.R., Bernard, A., Hawrylycz, M.J., Hof, P.R., Fischl, B., Lein, E.S., 2016. Comprehensive cellular-resolution atlas of the adult human brain. *J. Comp. Neurol.* 524, 3127–3481. <https://doi.org/10.1002/cne.24080>.
- Dinse, J., Härtwich, N., Waehnert, M.D., Tardif, C.L., Schäfer, A., Geyer, S., Preim, B., Turner, R., Bazin, P.L., 2015. A cytoarchitecture-driven myelin model reveals area-specific signatures in human primary and secondary areas using ultra-high resolution in-vivo brain MRI. *NeuroImage* 114, 71–87. <https://doi.org/10.1016/j.neuroimage.2015.04.023>.

- Does, M.D., 2018. Inferring brain tissue composition and microstructure via MR relaxometry. *NeuroImage* 182, 136–148.
- Draganski, B., May, A., 2008. Training-induced structural changes in the adult human brain. *Behav. Brain Res.* 192, 137–142. <https://doi.org/10.1016/j.bbr.2008.02.015>.
- Drobnjak, I., Zhang, H., Ianuş, A., Kaden, E., Alexander, D.C., 2016. PGSE, OGSE, and sensitivity to axon diameter in diffusion MRI: insight from a simulation study. *Magn. Reson. Med.* 75, 688–700. <https://doi.org/10.1002/mrm.25631>.
- Dumoulin, S.O., Harvey, B.M., Fracasso, A., Zuiderbaan, W., Luijten, P.R., Wandell, B.A., Petridou, N., 2017. In vivo evidence of functional and anatomical stripe-based subdivisions in human V2 and V3. *Sci. Rep.* 7, 733. <https://doi.org/10.1038/s41598-017-00634-6>.
- Dumoulin, S.O., Fracasso, A., van der Zwaag, W., Siero, J.C.W., Petridou, N., 2018. Ultra-high field MRI: advancing systems neuroscience towards mesoscopic human brain function. *NeuroImage* 168, 345–357. <https://doi.org/10.1016/j.neuroimage.2017.01.028>.
- Duvernoy, H.M., Delon, S., Vannson, J.L., 1981. Cortical blood vessels of the human brain. *Brain Res. Bull.* 7, 519–579. [https://doi.org/10.1016/0361-9230\(81\)90007-1](https://doi.org/10.1016/0361-9230(81)90007-1).
- Duyn, J.H., 2018. Studying brain microstructure with magnetic susceptibility contrast at high-field. *NeuroImage* 168, 152–161. <https://doi.org/10.1016/j.neuroimage.2017.02.046>.
- Duyn, J.H., Schenck, J., 2017. Contributions to magnetic susceptibility of brain tissue. *NMR Biomed.* 30, e3546. <https://doi.org/10.1002/nbm.3546>.
- Eickhoff, S., Walters, N.B., Schleicher, A., Kril, J., Egan, G.F., Zilles, K., Watson, J.D.G., Amunts, K., 2005. High-resolution MRI reflects myeloarchitecture and cytoarchitecture of human cerebral cortex. *Hum. Brain Mapp.* 24, 206–215. <https://doi.org/10.1002/hbm.20082>.
- Ellerbrock, I., Mohammadi, S., 2018a. Four in vivo g-ratio-weighted imaging methods: comparability and repeatability at the group level. *Hum. Brain Mapp.* 39, 24–41. <https://doi.org/10.1002/hbm.23858>. Corrigendum: Ellerbrock and Mohammadi (2018a).
- Ellerbrock, I., Mohammadi, S., 2018b. Corrigendum to Ellerbrock et al. (2018) “Four in vivo g-ratio-weighted imaging methods: comparability and repeatability at the group level”. *Hum. Brain Mapp.* 39. <https://doi.org/10.1002/hbm.23980>, 1467–1467.
- Farquharson, S., Tournier, J.D., 2016. High angular resolution diffusion imaging. In: Hecke, W.V., Emsell, L., Sunaert, S. (Eds.), *Diffusion Tensor Imaging*. Springer, New York, pp. 383–406. https://doi.org/10.1007/978-1-4939-3118-7_20.
- Feng, X., Deistung, A., Reichenbach, J.R., 2018. Quantitative susceptibility mapping (QSM) and R_2^* in the human brain at 3 T: Evaluation of intra-scanner repeatability. *Z. Med. Phys.* 28, 36–48. <https://doi.org/10.1016/j.zemedi.2017.05.003>.
- Fields, R.D., 2015. A new mechanism of nervous system plasticity: activity-dependent myelination. *Nat. Rev. Neurosci.* 16, 756–767. <https://doi.org/10.1038/nrn4023>.
- Fischl, B., Dale, A.M., 2000. Measuring the thickness of the human cerebral cortex from magnetic resonance images. *Proc. Natl. Acad. Sci.* 97, 11050–11055. <https://doi.org/10.1073/pnas.200033797>.
- Flechsig, P., 1920. *Anatomie des menschlichen Gehirns und Rückenmarks, vol. 1*. Verlag von Georg Thieme, Leipzig.
- Fonta, C., Imbert, M., 2002. Vascularization in the primate visual cortex during development. *Cereb. Cortex* 12, 199–211. <https://doi.org/10.1093/cercor/12.2.199>.
- Forstmann, B.U., de Hollander, G., van Maanen, L., Alkemade, A., Keuken, M.C., 2016. Towards a mechanistic understanding of the human subcortex. *Nat. Rev. Neurosci.* 18, 57–65. <https://doi.org/10.1038/nrn.2016.163>.
- Freund, P., Weiskopf, N., Ashburner, J., Wolf, K., Sutter, R., Altmann, D.R., Friston, K., Thompson, A., Curt, A., 2013. MRI investigation of the sensorimotor cortex and the corticospinal tract after acute spinal cord injury: a prospective longitudinal study. *Lancet Neurol.* 12, 873–881. [https://doi.org/10.1016/S1474-4422\(13\)70146-7](https://doi.org/10.1016/S1474-4422(13)70146-7).
- Fukunaga, M., Li, T.Q., van Gelderen, P., de Zwart, J.A., Shmueli, K., Yao, B., Lee, J., Maric, D., Aronova, M.A., Zhang, G., Leapman, R.D., Schenck, J.F., Merkle, H., Duyn, J.H., 2010. Layer-specific variation of iron content in cerebral cortex as a source of MRI contrast. *Proc. Natl. Acad. Sci.* 107, 3834–3839. <https://doi.org/10.1073/pnas.0911177107>.
- Fullerton, G.D., Potter, J.L., Dornbluth, N.C., 1982. NMR relaxation of protons in tissues and other macromolecular water solutions. *Magn. Reson. Imag.* 1, 209–226. [https://doi.org/10.1016/0730-725X\(82\)90172-2](https://doi.org/10.1016/0730-725X(82)90172-2).
- Geyer, S., Weiss, M., Reimann, K., Lohmann, G., Turner, R., 2011. Microstructural parcellation of the human cerebral cortex – from Brodmann's post-mortem map to in vivo mapping with high-field magnetic resonance imaging. *Front. Hum. Neurosci.* 5, 19. <https://doi.org/10.3389/fnhum.2011.00019>.
- Gil, R., Khabipova, D., Zwiers, M., Hilbert, T., Kober, T., Marques, J.P., 2016. An in vivo study of the orientation-dependent and independent components of transverse relaxation rates in white matter. *NMR Biomed.* 29, 1780–1790. <https://doi.org/10.1002/nbm.3616>.
- Glasser, M.F., Van Essen, D.C., 2011. Mapping human cortical areas in vivo based on myelin content as revealed by T1- and T2-weighted MRI. *J. Neurosci.* 31, 11597–11616. <https://doi.org/10.1523/JNEUROSCI.2180-11.2011>.
- Glasser, M.F., Sotiropoulos, S.N., Wilson, J.A., Coalson, T.S., Fischl, B., Andersson, J.L., Xu, J., Jbabdi, S., Webster, M., Polimeni, J.R., Essen, D.C.V., Jenkinson, M., 2013. The minimal preprocessing pipelines for the Human Connectome Project. *NeuroImage* 80, 105–124. <https://doi.org/10.1016/j.neuroimage.2013.04.127>.
- Glasser, M.F., Goyal, M.S., Preuss, T.M., Raichle, M.E., Van Essen, D.C., 2014. Trends and properties of human cerebral cortex: correlations with cortical myelin content. *NeuroImage* 93, 165–175. <https://doi.org/10.1016/j.neuroimage.2013.03.060>.
- Glasser, M.F., Coalson, T.S., Robinson, E.C., Hacker, C.D., Harwell, J., Yacoub, E., Ugurbil, K., Andersson, J., Beckmann, C.F., Jenkinson, M., Smith, S.M., Van Essen, D.C., 2016. A multi-modal parcellation of human cerebral cortex. *Nature* 536, 171–178. <https://doi.org/10.1038/nature18933>.
- Gomez, J., Barnett, M.A., Natu, V., Mezer, A., Palomero-Gallagher, N., Weiner, K.S., Amunts, K., Zilles, K., Grill-Spector, K., 2017. Microstructural proliferation in human cortex is coupled with the development of face processing. *Science* 355, 68–71. <https://doi.org/10.1126/science.aag0311>.
- Gossuin, Y., Roch, A., Muller, R.N., Gillis, P., 2000. Relaxation induced by ferritin and ferritin-like magnetic particles: the role of proton exchange. *Magn. Reson. Med.* 43, 237–243. [https://doi.org/10.1002/\(SICI\)1522-2594\(200002\)43:2<237::AID-MRM10>3.0.CO;2-5](https://doi.org/10.1002/(SICI)1522-2594(200002)43:2<237::AID-MRM10>3.0.CO;2-5).
- Gossuin, Y., Roch, A., Muller, R.N., Gillis, P., Lo Bue, F., 2002. Anomalous nuclear magnetic relaxation of aqueous solutions of ferritin: an unprecedented first-order mechanism. *Magn. Reson. Med.* 48, 959–964. <https://doi.org/10.1002/mrm.10316>.
- Gossuin, Y., Gillis, P., Muller, R.N., Hocq, A., 2007. Relaxation by clustered ferritin: a model for ferritin-induced relaxation in vivo. *NMR Biomed.* 20, 749–756. <https://doi.org/10.1002/nbm.1140>.
- Govindarajan, S.T., Cohen-Adad, J., Sormani, M.P., Fan, A.P., Louapre, C., Mainiero, C., 2015. Reproducibility of T_2^* mapping in the human cerebral cortex in vivo at 7 tesla MRI. *J. Magn. Reson. Imag.* 42, 290–296. <https://doi.org/10.1002/jmri.24789>.
- Grossman, E.J., Kirov, I.I., Gonen, O., Novikov, D.S., Davatz, M.S., Lui, Y.W., Grossman, R.I., Ingles, M., Fieremans, E., 2015. N-acetyl-aspartate levels correlate with intra-axonal compartment parameters from diffusion MRI. *NeuroImage* 118, 334–343. <https://doi.org/10.1016/j.neuroimage.2015.05.061>.
- Haacke, E.M., Cheng, N.Y.C., House, M.J., Liu, Q., Neelavalli, J., Ogg, R.J., Khan, A., Ayaz, M., Kirsch, W., Obenaus, A., 2005. Imaging iron stores in the brain using magnetic resonance imaging. *Magn. Reson. Imag.* 23, 1–25. <https://doi.org/10.1016/j.mri.2004.10.001>.
- Haast, R.A.M., Ivanov, D., Formisano, E., Uludağ, K., 2016. Reproducibility and reliability of quantitative and weighted T_1 and T_2^* mapping for myelin-based cortical parcellation at 7 tesla. *Front. Neuroanat.* 10. <https://doi.org/10.3389/fnana.2016.00112>.
- Hallgren, B., Sourander, P., 1958. The effect of age on the non-haem iron in the human brain. *J. Neurochem.* 3, 41–51. <https://doi.org/10.1111/j.1471-4159.1958.tb12607.x>.
- Hamilton, J., Franson, D., Seiberlich, N., 2017. Recent advances in parallel imaging for MRI. *Prog. Nucl. Magn. Reson. Spectrosc.* 101, 71–95. <https://doi.org/10.1016/j.pnmrs.2017.04.002>.
- Hare, D.J., New, E.J., de Jonge, M.D., McColl, G., 2015. Imaging metals in biology: balancing sensitivity, selectivity and spatial resolution. *Chem. Soc. Rev.* 44, 5941–5958. <https://doi.org/10.1039/C5CS00055F>.
- Hayes, T.L., Lewis, D.A., 1996. Magnopyramidal neurons in the anterior motor speech region: dendritic features and interhemispheric comparisons. *Arch. Neurol.* 53, 1277–1283. <https://doi.org/10.1001/archneur.1996.00550120089021>.
- Helbling, S., Teki, S., Callaghan, M.F., Sedley, W., Mohammadi, S., Griffiths, T.D., Weiskopf, N., Barnes, G.R., 2015. Structure predicts function: combining non-invasive electrophysiology with in-vivo histology. *NeuroImage* 108, 377–385. <https://doi.org/10.1016/j.neuroimage.2014.12.030>.
- Hellwig, B., 1993. How the myelin picture of the human cerebral cortex can be computed from cytoarchitectural data. A bridge between von Economo and Vogt. *J. Hirnforsch.* 34, 387–402.
- Hellwig, B., 2002. Cyto- and myeloarchitectonics: their relationship and possible functional significance. In: Schüz and Miller (2002), pp. 15–28. chapter 2.
- Helms, G., Dath, H., Kallenberg, K., Dechent, P., 2008. High-resolution maps of magnetization transfer with inherent correction for RF inhomogeneity and T_1 relaxation obtained from 3D FLASH MRI. *Magn. Reson. Med.* 60, 1396–1407. <https://doi.org/10.1002/mrm.21732>.
- Henning, A., March 2018. Proton and multinuclear magnetic resonance spectroscopy in the human brain at ultra-high field strength: a review. *NeuroImage* 168, 181–198. <https://doi.org/10.1016/j.neuroimage.2017.07.017>.
- Hilgetag, C.C., Amunts, K., 2016. Connectivity and cortical architecture. *e-Neuroforum* 7, 56–63. <https://doi.org/10.1007/s13295-016-0028-0>.
- Hirsch, S., Reichold, J., Schneider, M., Székely, G., Weber, B., 2012. Topology and hemodynamics of the cortical cerebrovascular system. *J. Cereb. Blood Flow Metab.* 32, 952–967. <https://doi.org/10.1038/jcbfm.2012.39>.
- Hiscox, L.V., Johnson, C.L., Barnhill, E., McGarry, M.D.J., Huston 3rd, J., van Beek, E.J.R., Starr, J.M., Roberts, N., 2016. Magnetic resonance elastography (MRE) of the human brain: technique, findings and clinical applications. *Phys. Med. Biol.* 61, R401. <https://doi.org/10.1088/0031-9155/61/24/R401>.
- Hocq, A., Luhmer, M., Saussez, S., Louryan, S., Gillis, P., Gossuin, Y., 2015. Effect of magnetic field and iron content on NMR proton relaxation of liver, spleen and brain tissues. *Contrast Media Mol. Imaging* 10, 144–152. <https://doi.org/10.1002/cmml.1610>.
- Horsfield, M.A., Jones, D.K., 2002. Applications of diffusion-weighted and diffusion tensor MRI to white matter diseases – a review. *NMR Biomed.* 15, 570–577. <https://doi.org/10.1002/nbm.787>.
- Horton, J.C., 1984. Cytochrome oxidase patches: a new cytoarchitectonic feature of monkey visual cortex. *Phil. Trans. Roy. Soc. Lond. Ser. B Biol. Sci.* 304, 199–253. <https://doi.org/10.1098/rstb.1984.0021>.
- Horton, J.C., Adams, D.L., 2005. The cortical column: a structure without a function. *Phil. Trans. Roy. Soc. Lond. B Biol. Sci.* 360, 837–862. <https://doi.org/10.1098/rstb.2005.1623>.
- Huber, L., Handwerker, D.A., Jangraw, D.C., Chen, G., Hall, A., Stüber, C., Gonzalez-Castillo, J., Ivanov, D., Marrett, S., Guidi, M., Goense, J., Poser, B.A., Bandettini, P.A., 2017a. High-resolution CBV-fMRI allows mapping of laminar activity and connectivity of cortical input and output in human M1. *Neuron* 96, 1253–1263 e6. <https://doi.org/10.1016/j.neuron.2017.11.005>.

- Huber, L., Uludağ, K., Möller, H.E., 2017b. Non-BOLD contrast for laminar fMRI in humans: CBF, CBV, and CMR02. *NeuroImage*. <https://doi.org/10.1016/j.neuroimage.2017.07.041> (in press).
- Huntenburg, J.M., Bazin, P.L., Goulas, A., Tardif, C.L., Villringer, A., Margulies, D.S., 2017. A systematic relationship between functional connectivity and intracortical myelin in the human cerebral cortex. *Cereb. Cortex* 27, 981–997. <https://doi.org/10.1093/cercor/bhx030>.
- Ianus, A., Shemesh, N., Alexander, D.C., Drobnyak, I., 2017. Double oscillating diffusion encoding and sensitivity to microscopic anisotropy. *Magn. Reson. Med.* 78, 550–564. <https://doi.org/10.1002/mrm.26393>.
- Jack, C.R., Wengenack, T.M., Reyes, D.A., Garwood, M., Curran, G.L., Borowski, B.J., Lin, J., Preboske, G.M., Holasek, S.S., Adriany, G., Poduslo, J.F., 2005. In vivo magnetic resonance microimaging of individual amyloid plaques in Alzheimer's transgenic mice. *J. Neurosci.* 25, 10041–10048. <https://doi.org/10.1523/JNEUROSCI.2588-05.2005>.
- Jacobs, B., Scheibel, A.B., 2002. Regional dendritic variation in primate cortical pyramidal cells. in: Schüz and Müller (2002). chapter 6, pp. 111–131.
- Jespersen, S.N., Kroenke, C.D., Østergaard, L., Ackerman, J.J., Yablonskiy, D.A., 2007. Modeling dendrite density from magnetic resonance diffusion measurements. *NeuroImage* 34, 1473–1486. <https://doi.org/10.1016/j.neuroimage.2006.10.037>.
- Jespersen, S.N., Leigland, L.A., Cornea, A., Kroenke, C.D., 2012. Determination of axonal and dendritic orientation distributions within the developing cerebral cortex by diffusion tensor imaging. *IEEE Trans. Med. Imag.* 31, 16–32. <https://doi.org/10.1109/TMI.2011.2162099>.
- Jeurissen, B., Tournier, J.D., Dhollander, T., Connelly, A., Sijbers, J., 2014. Multi-tissue constrained spherical deconvolution for improved analysis of multi-shell diffusion MRI data. *NeuroImage* 103, 411–426. <https://doi.org/10.1016/j.neuroimage.2014.07.061>.
- Jin, T., Wang, P., Zong, X., Kim, S.G., 2013. MR imaging of the amide-proton transfer effect and the pH-insensitive nuclear overhauser effect at 9.4 T. *Magn. Reson. Med.* 69, 760–770. <https://doi.org/10.1002/mrm.24315>.
- Johnson, C.L., Telzer, E.H., 2017. Magnetic resonance elastography for examining developmental changes in the mechanical properties of the brain. *Dev. Cogn. Neurosci.* <https://doi.org/10.1016/j.dcn.2017.08.010> (in press).
- Jones, D.K. (Ed.), 2011. *Diffusion MRI: Theory, Methods, and Applications*. OUP, Oxford.
- Jung, W., Lee, J., Shin, H.G., Nam, Y., Zhang, H., Oh, S.H., Lee, J., 2018. Whole brain g-ratio mapping using myelin water imaging (MWI) and neurite orientation dispersion and density imaging (NODDI). *NeuroImage* 182, 379–388.
- Kasthuri, N., Hayworth, K.J., Berger, D.R., Schalek, R.L., Conchello, J.A., Knowles-Barley, S., Lee, D., Vázquez-Reina, A., Kaynig, V., Jones, T.R., Roberts, M., Morgan, J.L., Tapia, J.C., Seung, H.S., Roncal, W.G., Vogelstein, J.T., Burns, R., Sussman, D.L., Priebe, C.E., Pfister, H., Lichtman, J.W., 2015. Saturated reconstruction of a volume of neocortex. *Cell* 162, 648–661. <https://doi.org/10.1016/j.cell.2015.06.054>.
- Keller, A.L., Schüz, A., Logothetis, N.K., Weber, B., 2011. Vascularization of cytochrome oxidase-rich blobs in the primary visual cortex of squirrel and macaque monkeys. *J. Neurosci.* 31, 1246–1253. <https://doi.org/10.1523/JNEUROSCI.2765-10.2011>.
- Kettenmann, H., Verkhratsky, A., 2011. Neuroglia, der lebende Nervenkitzel. *Fortschr. Neurol. Psychiatr.* 79, 588–597. <https://doi.org/10.1055/s-0031-1281704>.
- Khakh, B.S., Sofroniew, M.V., 2015. Diversity of astrocyte functions and phenotypes in neural circuits. *Nat. Neurosci.* 18, 942. <https://doi.org/10.1038/nn.4043>.
- Kim, S.G., Knösche, T.R., 2016. Intracortical myelination in musicians with absolute pitch: quantitative morphometry using 7-T MRI. *Hum. Brain Mapp.* 37, 3486–3501. <https://doi.org/10.1002/hbm.23254>.
- Kiselev, V.G., Novikov, D.S., 2002. Transverse NMR relaxation as a probe of mesoscopic structure. *Phys. Rev. Lett.* 89, 278101. <https://doi.org/10.1103/PhysRevLett.89.278101>.
- Kleinnijenhuis, M., van Mourik, T., Norris, D.G., Ruiter, D.J., van Cappellen van Walsum, A.M., Barth, M., 2015. Diffusion tensor characteristics of gyrencephaly using high resolution diffusion MRI in vivo at 7T. *NeuroImage* 109, 378–387. <https://doi.org/10.1016/j.neuroimage.2015.01.001>.
- Knight, M.J., Kauppinen, R.A., 2016. Diffusion-mediated nuclear spin phase decoherence in cylindrically porous materials. *J. Magn. Reson.* 269, 1–12. <https://doi.org/10.1016/j.jmr.2016.05.007>.
- Koenig, S.H., 1991. Cholesterol of myelin is the determinant of gray-white contrast in MRI of brain. *Magn. Reson. Med.* 20, 285–291. <https://doi.org/10.1002/mrm.1910200210.abstract>.
- Koopmans, P.J., Mannesing, R., Niessen, W.J., Viergever, M.A., Barth, M., 2008. MR venography of the human brain using susceptibility weighted imaging at very high field strength. *Magn. Reson. Mater. Phys. Biol. Med.* 21, 149. <https://doi.org/10.1007/s10334-007-0101-3>.
- Kucharczyk, W., Macdonald, P.M., Stanisz, G.J., Henkelman, R.M., 1994. Relaxivity and magnetization transfer of white matter lipids at MR imaging: importance of cerebrospines and pH. *Radiology* 192, 521–529. <https://doi.org/10.1148/radiology.192.2.8029426>.
- Kuehn, E., Dinse, J., Jakobsen, E., Long, X., Schäfer, A., Bazin, P.L., Villringer, A., Sereno, M.I., Margulies, D.S., 2017. Body topography parcellates human sensory and motor cortex. *Cereb. Cortex* 27, 3790–3805. <https://doi.org/10.1093/cercor/bhx026>.
- Kwan, J.Y., Jeong, S.Y., Gelderen, P.V., Deng, H.X., Quezado, M.M., Danielian, L.E., Butman, J.A., Chen, L., Bayat, E., Russell, J., Siddique, T., Duyn, J.H., Rouault, T.A., Floeter, M.K., 2012. Iron accumulation in deep cortical layers accounts for MRI signal abnormalities in ALS: correlating 7 tesla MRI and pathology. *PLoS One* 7, e35241. <https://doi.org/10.1371/journal.pone.0035241>.
- Langkammer, C., Krebs, N., Goessler, W., Scheurer, E., Ebner, F., Yen, K., Fazekas, F., Ropele, S., 2010. Quantitative MR imaging of brain iron: a postmortem validation study. *Radiology* 257, 455–462. <https://doi.org/10.1148/radiol.10100495>.
- Langkammer, C., Schweser, F., Krebs, N., Deistung, A., Goessler, W., Scheurer, E., Sommer, K., Reishofer, G., Yen, K., Fazekas, F., Ropele, S., Reichenbach, J.R., 2012. Quantitative susceptibility mapping (QSM) as a means to measure brain iron? A post mortem validation study. *NeuroImage* 62, 1593–1599. <https://doi.org/10.1016/j.neuroimage.2012.05.049>.
- Larkman, D.J., Nunes, R.G., 2007. Parallel magnetic resonance imaging. *Phys. Med. Biol.* 52, R15. <https://doi.org/10.1088/0031-9155/52/7/R01>.
- Laule, C., Vavasour, I.M., Kolind, S.H., Li, D.K.B., Trabulsee, T.L., Moore, G.R.W., MacKay, A.L., 2007. Magnetic resonance imaging of myelin. *Neurotherapeutics* 4, 460–484. <https://doi.org/10.1016/j.nurt.2007.05.004>.
- Lawrence, S.J.D., Formisano, E., Muckli, L., de Lange, F.P., 2017. Laminar fMRI: applications for cognitive neuroscience. *NeuroImage*. <https://doi.org/10.1016/j.neuroimage.2017.07.004> (in press).
- Lerch, J.P., van der Kouwe, A.J.W., Raznahan, A., Paus, T., Johansen-Berg, H., Miller, K.L., Smith, S.M., Fischl, B., Sotiropoulos, S.N., 2017. Studying neuroanatomy using MRI. *Nat. Neurosci.* 20, 314–326. <https://doi.org/10.1038/nn.4501>.
- Leuze, C.W.U., Anwender, A., Bazin, P.L., Dhital, B., Stüber, C., Reimann, K., Geyer, S., Turner, R., 2014. Layer-specific intracortical connectivity revealed with diffusion MRI. *Cereb. Cortex* 24, 328–339. <https://doi.org/10.1093/cercor/bhs311>.
- Leuze, C., Aswendt, M., Ferenczi, E., Liu, C.W., Hsueh, B., Goubran, M., Tian, Q., Steinberg, G., Zeineh, M.M., Deisseroth, K., McNab, J.A., 2017. The separate effects of lipids and proteins on brain MRI contrast revealed through tissue clearing. *NeuroImage* 156, 412–422. <https://doi.org/10.1016/j.neuroimage.2017.04.021>.
- Liewald, D., Miller, R., Logothetis, N., Wagner, H.J., Schüz, A., 2014. Distribution of axon diameters in cortical white matter: an electron-microscopic study on three human brains and a macaque. *Biol. Cybern.* 108, 541–557. <https://doi.org/10.1007/s00422-014-0626-2>.
- Lifshits, S., Tomer, O., Shamir, I., Barazany, D., Tsarfaty, G., Rosset, S., Assaf, Y., 2018. Resolution considerations in imaging of the cortical layers. *NeuroImage* 164, 112–120. <https://doi.org/10.1016/j.neuroimage.2017.02.086>.
- Lorio, S., Kherif, F., Ruef, A., Melie-Garcia, L., Frackowiak, R., Ashburner, J., Helms, G., Lutti, A., Draganski, B., 2016. Neurobiological origin of spurious brain morphological changes: a quantitative MRI study. *Hum. Brain Mapp.* 37, 1801–1815. <https://doi.org/10.1002/hbm.23137>.
- Luders, E., Thompson, P.M., Narr, K.L., Toga, A.W., Jancke, L., Gaser, C., 2006. A curvature-based approach to estimate local gyrification on the cortical surface. *NeuroImage* 29, 1224–1230. <https://doi.org/10.1016/j.neuroimage.2005.08.049>.
- Lüsebrink, F., Sciarra, A., Mattem, H., Yakupov, R., Speck, O., 2017. T₁-weighted in vivo human whole brain MRI dataset with an ultrahigh isotropic resolution of 250 μ m. *Sci. Data* 4, sdata201732. <https://doi.org/10.1038/sdata.2017.32>.
- Lustig, M., Donoho, D., Pauly, J.M., 2007. Sparse MRI: the application of compressed sensing for rapid MRI imaging. *Magn. Reson. Med.* 58, 1182–1195. <https://doi.org/10.1002/mrm.21391>.
- Lustig, M., Donoho, D.L., Santos, J.M., Pauly, J.M., 2008. Compressed sensing MRI. *IEEE Signal Process. Mag.* 25, 72–82. <https://doi.org/10.1109/MSP.2007.914728>.
- Lutti, A., Dick, F., Sereno, M.I., Weiskopf, N., 2014. Using high-resolution quantitative mapping of R1 as an index of cortical myelination. *NeuroImage* 93 (Pt 2), 176–188. <https://doi.org/10.1016/j.neuroimage.2013.06.005>.
- MacKay, A., Laule, C., Vavasour, I., Bjarnason, T., Kolind, S., Mädlar, B., 2006. Insights into brain microstructure from the T₂ distribution. *Magn. Reson. Imag.* 24, 515–525. <https://doi.org/10.1016/j.mri.2005.12.037>.
- Magerkurth, J., Volz, S., Wagner, M., Jurcoane, A., Anti, S., Seiler, A., Hattingen, E., Deichmann, R., 2011. Quantitative T₂*-mapping based on multi-slice multiple gradient echo flash imaging: retrospective correction for subject motion effects. *Magn. Reson. Med.* 66, 989–997. <https://doi.org/10.1002/mrm.22878>.
- Mangate, G., Govindarajan, S.T., Mainiero, C., Cohen-Adad, J., 2015. Multivariate combination of magnetization transfer, T₂* and B0 orientation to study the myelo-architecture of the in vivo human cortex. *NeuroImage* 119, 89–102. <https://doi.org/10.1016/j.neuroimage.2015.06.033>.
- Marques, J.P., Khabipova, D., Gruetter, R., 2017. Studying cyto and myeloarchitecture of the human cortex at ultra-high field with quantitative imaging: R1, R2* and magnetic susceptibility. *NeuroImage* 147, 152–163. <https://doi.org/10.1016/j.neuroimage.2016.12.009>.
- McCarthy, M.M., 2017. Location, location, location: microglia are where they live. *Neuron* 95, 233–235. <https://doi.org/10.1016/j.neuron.2017.07.005>.
- McGarry, M., Johnson, C.L., Sutton, B.P., Van Houten, E.E.W., Georgiadis, J.G., Weaver, J.B., Paulsen, K.D., 2013. Including spatial information in nonlinear inversion MR elastography using soft prior regularization. *IEEE Trans. Med. Imag.* 32, 1901–1909. <https://doi.org/10.1109/TMI.2013.2268978>.
- McNab, J.A., Polimeni, J.R., Wang, R., Augustinack, J.C., Fujimoto, K., Stevens, A., Janssens, T., Parivar, R., Folkerth, R.D., Vanduffel, W., Wald, L.L., 2013. Surface based analysis of diffusion orientation for identifying architectonic domains in the in vivo human cortex. *NeuroImage* 69, 87–100. <https://doi.org/10.1016/j.neuroimage.2012.11.065>.
- Meadowcroft, M.D., Peters, D.G., Connor, J.R., Yang, Q.X., 2015. The effect of iron in MRI and transverse relaxation of amyloid-beta plaques in Alzheimer's disease. *NMR Biomed.* 28, 297–305. <https://doi.org/10.1002/nbm.3247>.
- Mechelli, A., Price, C.J., Friston, K.J., Ashburner, J., 2005. Voxel-based morphometry of the human brain: methods and applications. *Curr. Med. Imag. Rev.* 1, 105–113. <https://doi.org/10.2174/1573405050438726>.
- Meter, R., Kober, T., Möller, H.E., Schäfer, A., 2017. Simultaneous quantitative MRI mapping of T₁, T₂* and magnetic susceptibility with multi-echo MP2RAGE. *PLoS One* 12. <https://doi.org/10.1371/journal.pone.0169265>.

- Meyers, S.M., Kolind, S.H., MacKay, A.L., 2017. Simultaneous measurement of total water content and myelin water fraction in brain at 3T using a T₂ relaxation based method. *Magn. Reson. Imaging* 37, 187–194. <https://doi.org/10.1016/j.mri.2016.12.001>.
- Mezer, A., Yeatman, J.D., Stikov, N., Kay, K.N., Cho, N.J., Dougherty, R.F., Perry, M.L., Parvizi, J., Hua, L.H., Butts-Pauly, K., Wandell, B.A., 2013. Quantifying the local tissue volume and composition in individual brains with magnetic resonance imaging. *Nat. Med.* 19, 1667–1672. <https://doi.org/10.1038/nm.3390>.
- Micheva, K.D., Wolman, D., Mensh, B.D., Pax, E., Buchanan, J., Smith, S.J., Bock, D.D., 2016. A large fraction of neocortical myelin ensheathes axons of local inhibitory neurons. *eLife* 5, e15784. <https://doi.org/10.7554/eLife.15784>.
- Mohammadi, S., Tabelow, K., Ruthotto, L., Feiweier, T., Polzehl, J., Weiskopf, N., 2015. High-resolution diffusion kurtosis imaging at 3T enabled by advanced post-processing. *Front. Neurosci.* 8 <https://doi.org/10.3389/fnins.2014.00427>.
- Morawski, M., Reinert, T., Meinecke, C., Arendt, T., Butz, T., 2005. Antibody meets the microbeam – or how to find neurofibrillary tangles. *Nucl. Instrum. Methods Phys. Res. Sect. B Beam Interact. Mater. Atoms* 231, 229–233. <https://doi.org/10.1016/j.nimb.2005.01.062>.
- Morawski, M., Kirilina, E., Scherf, N., Jäger, C., Reimann, K., Trampel, R., Gavrilidis, F., Geyer, S., Biedermann, B., Arendt, T., Weiskopf, N., 2018. Developing 3D microscopy with CLARITY on human brain tissue: Towards a tool for informing and validating MRI-based histology. *NeuroImage* 182, 417–428.
- Morell, P., Quarles, R.H., Norton, W.T., 1994. Myelin formation, structure, and biochemistry. In: Siegel, G.J., Agranoff, B.W., Albers, R.W., Molinoff, P.B. (Eds.), *Basic Neurochemistry, fifth ed.* Raven Press, New York, chapter 6, pp. 117–143.
- Morris, C.M., Candy, J.M., Oakley, A.E., Bloxham, C.A., Edwardson, J.A., 1992. Histochemical distribution of non-haem iron in the human brain. *Cells Tissues Organs* 144, 235–257. <https://doi.org/10.1159/000147312>.
- Morris, K., Kundu, P., Dowell, N., Mechelmans, D.J., Favre, P., Irvine, M.A., Robbins, T.W., Daw, N., Bullmore, E.T., Harrison, N.A., Voon, V., 2016. Frontostriatal organization: defining functional and microstructural substrates of behavioural flexibility. *Cortex* 74, 118–133. <https://doi.org/10.1016/j.cortex.2015.11.004>.
- Mougin, O., Clemence, M., Peters, A., Pitiot, A., Gowland, P., 2013. High-resolution imaging of magnetisation transfer and nuclear Overhauser effect in the human visual cortex at 7 T. *NMR Biomed.* 26, 1508–1517. <https://doi.org/10.1002/nbm.2984>.
- Muthupillai, R., Lomas, D.J., Rossman, P.J., Greenleaf, J.F., Manduca, A., Ehman, R.L., 1995. Magnetic resonance elastography by direct visualization of propagating acoustic strain waves. *Science* 269, 1854–1857. <https://doi.org/10.1126/science.7569924>.
- Nagy, Z., Alexander, D.C., Thomas, D.L., Weiskopf, N., Sereno, M.I., 2013. Using high angular resolution diffusion imaging data to discriminate cortical regions. *PLoS One* 8, e63842. <https://doi.org/10.1371/journal.pone.0063842>.
- Nair, G., Tanahashi, Y., Low, H.P., Billings-Gagliardi, S., Schwartz, W.J., Duong, T.Q., 2005. Myelination and long diffusion times alter diffusion-tensor-imaging contrast in myelin-deficient shiverer mice. *NeuroImage* 28, 165–174. <https://doi.org/10.1016/j.neuroimage.2005.05.049>.
- Najac, C., Branzoli, F., Ronen, I., Valette, J., 2016. Brain intracellular metabolites are freely diffusing along cell fibers in grey and white matter, as measured by diffusion-weighted MR spectroscopy in the human brain at 7 T. *Brain Struct. Funct.* 221, 1245–1254. <https://doi.org/10.1007/s00429-014-0968-5>.
- Nasr, S., Polimeni, J.R., Tootell, R.B.H., 2016. Interdigitated color- and disparity-selective columns within human visual cortical areas V2 and V3. *J. Neurosci.* 36, 1841–1857. <https://doi.org/10.1523/JNEUROSCI.3518-15.2016>.
- Nazeri, A., Chakravarty, M.M., Rotenberg, D.J., Rajji, T.K., Rath, Y., Michailovich, O.V., Voineskos, A.N., 2015. Functional consequences of neurite orientation dispersion and density in humans across the adult lifespan. *J. Neurosci.* 35, 1753–1762. <https://doi.org/10.1523/JNEUROSCI.3979-14.2015>.
- Nieuwenhuys, R., Broere, C.A.J., 2017. A map of the human neocortex showing the estimated overall myelin content of the individual architectonic areas based on the studies of Adolf Hopf. *Brain Struct. Funct.* 222, 465–480. <https://doi.org/10.1007/s00429-016-1228-7>.
- Nieuwenhuys, R., Voogd, J., van Huijzen, C., 2008. *The Human central Nervous System*. Springer, Berlin.
- Nieuwenhuys, R., Broere, C.A.J., Cerliani, L., 2015a. A new myeloarchitectonic map of the human neocortex based on data from the Vogt–Vogt school. *Brain Struct. Funct.* 220, 2551–2573. <https://doi.org/10.1007/s00429-014-0806-9>. Erratum: Nieuwenhuys et al. (2015a).
- Nieuwenhuys, R., Broere, C.A.J., Cerliani, L., 2015b. Erratum to: a new myeloarchitectonic map of the human neocortex based on data from the Vogt–Vogt school. *Brain Struct. Funct.* 220, 3753–3755. <https://doi.org/10.1007/s00429-014-0884-8>.
- Nilsson, M., Lasić, S., Drobniak, I., Topgaard, D., Westin, C.F., 2017. Resolution limit of cylinder diameter estimation by diffusion MRI: the impact of gradient waveform and orientation dispersion. *NMR Biomed.* 30, e3711. <https://doi.org/10.1002/nbm.3711>.
- Nöth, U., Hattingsen, E., Bähr, O., Tichy, J., Deichmann, R., 2015. Improved visibility of brain tumors in synthetic MP-RAGE anatomies with pure T₁ weighting. *NMR Biomed.* 28, 818–830. <https://doi.org/10.1002/nbm.3324>.
- Novikov, D.S., Jensen, J.H., Helpert, J.A., Fieremans, E., 2014. Revealing mesoscopic structural universality with diffusion. *Proc. Natl. Acad. Sci.* 111, 5088–5093. <https://doi.org/10.1073/pnas.1316944111>.
- Novikov, D.S., Jespersen, S.N., Kiselev, V.G., Fieremans, E., 2016. Quantifying Brain Microstructure with Diffusion MRI: Theory and Parameter Estimation. *arXiv: 1612.02059 [physics]*.
- O'Callaghan, J., Holmes, H., Powell, N., Wells, J.A., Ismail, O., Harrison, I.F., Siow, B., Johnson, R., Ahmed, Z., Fisher, A., Meftah, S., O'Neill, M.J., Murray, T.K., Collins, E.C., Shmueli, K., Lythgoe, M.F., 2017. Tissue magnetic susceptibility mapping as a marker of tau pathology in Alzheimer's disease. *NeuroImage* 159, 334–345. <https://doi.org/10.1016/j.neuroimage.2017.08.003>.
- Oberheim, N.A., Wang, X., Goldman, S., Nedergaard, M., 2006. Astrocytic complexity distinguishes the human brain. *Trends Neurosci.* 29, 547–553. <https://doi.org/10.1016/j.tins.2006.08.004>.
- Ono, M., Kubik, S., Abernathy, C.D., 1990. *Atlas of the Cerebral Sulci*. Georg Thieme Verlag, Stuttgart.
- Palombo, M., Ligneul, C., Najac, C., Douce, J.L., Flament, J., Escartin, C., Hantraye, P., Brouillet, E., Bonvento, G., Valette, J., 2016. New paradigm to assess brain cell morphology by diffusion-weighted MR spectroscopy in vivo. *Proc. Natl. Acad. Sci.* 113, 6671–6676. <https://doi.org/10.1073/pnas.1504327113>.
- Palombo, M., Shemesh, N., Ronen, I., Valette, J., 2018. Insights into brain microstructure from in vivo DW-MRS. *NeuroImage* 182, 97–116.
- Palomero-Gallagher, N., Zilles, K., 2017. Cortical layers: cyto-, myelo-, receptor- and synaptic architecture in human cortical areas. *NeuroImage*. <https://doi.org/10.1016/j.neuroimage.2017.08.035> (in press).
- Pampel, A., Müller, D.K., Anwender, A., Marschner, H., Möller, H.E., 2015. Orientation dependence of magnetization transfer parameters in human white matter. *NeuroImage* 114, 136–146. <https://doi.org/10.1016/j.neuroimage.2015.03.068>.
- Pasternak, O., Sochen, N., Gur, Y., Intrator, N., Assaf, Y., 2009. Free water elimination and mapping from diffusion MRI. *Magn. Reson. Med.* 62, 717–730. <https://doi.org/10.1002/mrm.22055>.
- Pike, G.B., 1996. Pulsed magnetization transfer contrast in gradient echo imaging: a two-pool analytic description of signal response. *Magn. Reson. Med.* 36, 95–103. <https://doi.org/10.1002/mrm.1910360117>.
- Quintana, C., Bellefiqu, S., Laval, J.Y., Guerquin-Kern, J.L., Wu, T.D., Avila, J., Ferrer, I., Arranz, R., Patiño, C., 2006. Study of the localization of iron, ferritin, and hemosiderin in Alzheimer's disease hippocampus by analytical microscopy at the subcellular level. *J. Struct. Biol.* 153, 42–54. <https://doi.org/10.1016/j.jsb.2005.11.001>.
- Rademacher, J., 2002. Topographical variability of cytoarchitectonic areas. In: Schüz and Miller (2002), chapter 4, pp. 53–78.
- Rakic, P., 1988. Specification of cerebral cortical areas. *Science* 241, 170–176. <https://doi.org/10.1126/science.3291116>.
- Rathi, Y., Pasternak, O., Savadjiev, P., Michailovich, O., Bouix, S., Kubicki, M., Westin, C.F., Makris, N., Shenton, M., 2014. Gray matter alterations in early aging: a diffusion magnetic resonance imaging study. *Hum. Brain Mapp.* 35, 3841–3856. <https://doi.org/10.1002/hbm.22441>.
- Rockland, K.S., 2017. What do we know about laminar connectivity? *NeuroImage*. <https://doi.org/10.1016/j.neuroimage.2017.07.032> (in press).
- Ross, B., Bluml, S., 2001. Magnetic resonance spectroscopy of the human brain. *Anat. Rec.* 265, 54–84. <https://doi.org/10.1002/ar.1058>.
- Rowley, C.D., Sehmbi, M., Bazin, P.L., Tardif, C.L., Minuzzi, L., Frey, B.N., Bock, N.A., 2017. Age-related mapping of intracortical myelin from late adolescence to middle adulthood using T₁-weighted MRI. *Hum. Brain Mapp.* 38, 3691–3703. <https://doi.org/10.1002/hbm.23624>.
- Ruthotto, L., Kugel, H., Olesch, J., Fischer, B., Modersitzki, J., Burger, M., Wolters, C.H., 2012. Diffeomorphic susceptibility artifact correction of diffusion-weighted magnetic resonance images. *Phys. Med. Biol.* 57, 5715. <https://doi.org/10.1088/0031-9155/57/18/5715>.
- Ruthotto, L., Mohammadi, S., Weiskopf, N., 2014. A new method for joint susceptibility artefact correction and super-resolution for dMRI. In: *Medical Imaging 2014: Image Processing*, p. 90340P. <https://doi.org/10.1117/12.2043591>.
- Sánchez-Panchuelo, R.M., Francis, S.T., Schluppeck, D., Bowtell, R.W., 2012. Correspondence of human visual areas identified using functional and anatomical MRI in vivo at 7 T. *J. Magn. Reson. Imaging* 35, 287–299. <https://doi.org/10.1002/jmri.22822>.
- Schmid, F., Barrett, M.J.P., Jenny, P., Weber, B., 2017. Vascular density and distribution in neocortex. *NeuroImage*. <https://doi.org/10.1016/j.neuroimage.2017.06.046> (in press).
- Schmierer, K., Scaravilli, F., Altmann, D.R., Barker, G.J., Miller, D.H., 2004. Magnetization transfer ratio and myelin in postmortem multiple sclerosis brain. *Ann. Neurol.* 56, 407–415. <https://doi.org/10.1002/ana.20202>.
- Schmierer, K., Wheeler-Kingshott, C.A.M., Tozer, D.J., Boulby, P.A., Parkes, H.G., Yousry, T.A., Scaravilli, F., Barker, G.J., Tofts, P.S., Miller, D.H., 2008. Quantitative magnetic resonance of postmortem multiple sclerosis brain before and after fixation. *Magn. Reson. Med.* 59, 268–277. <https://doi.org/10.1002/mrm.21487>.
- Schmierer, K., Thavarajah, J.R., An, S.F., Brandner, S., Miller, D.H., Tozer, D.J., 2010. Effects of formalin fixation on magnetic resonance indices in multiple sclerosis cortical gray matter. *J. Magn. Reson. Imaging* 32, 1054–1060. <https://doi.org/10.1002/jmri.22381>.
- Scholtens, L.H., de Reus, M.A., van den Heuvel, M.P., 2015. Linking contemporary high resolution magnetic resonance imaging to the von Economo legacy: a study on the comparison of MRI cortical thickness and histological measurements of cortical structure. *Hum. Brain Mapp.* 36, 3038–3046. <https://doi.org/10.1002/hbm.22826>.
- Schüz, A., Miller, R. (Eds.), 2002. *Cortical Areas: Unity and Diversity. Volume 5 of Conceptual Advances in Brain Research*. Taylor & Francis, New York.
- Schweser, F., Deistung, A., Lehr, B.W., Reichenbach, J.R., 2011. Quantitative imaging of intrinsic magnetic tissue properties using MRI signal phase: an approach to in vivo brain iron metabolism? *NeuroImage* 54, 2789–2807. <https://doi.org/10.1016/j.neuroimage.2010.10.070>.

- Sereno, M.I., Dale, A.M., Reppas, J.B., Kwong, K.K., Belliveau, J.W., Brady, T.J., Rosen, B.R., Tootell, R.B., 1995. Borders of multiple visual areas in humans revealed by functional magnetic resonance imaging. *Science* 268, 889–893. <https://doi.org/10.1126/science.7754376>.
- Sereno, M.I., Lutti, A., Weiskopf, N., Dick, F., 2013. Mapping the human cortical surface by combining quantitative T_1 with retinotopy. *Cereb. Cortex* 23, 2261–2268. <https://doi.org/10.1093/cercor/bhs213>.
- Setsompop, K., Kimmlingen, R., Eberlein, E., Witzel, T., Cohen-Adad, J., McNab, J.A., Keil, B., Tisdall, M.D., Hoecht, P., Dietz, P., Cauley, S.F., Tountcheva, V., Matschl, V., Lenz, V.H., Heberlein, K., Potthast, A., Thein, H., Van Horn, J., Toga, A., Schmitt, F., Lehne, D., Rosen, B.R., Wedeen, V., Wald, L.L., 2013. Pushing the limits of in vivo diffusion MRI for the human connectome project. *NeuroImage* 80, 220–233. <https://doi.org/10.1016/j.neuroimage.2013.05.078>.
- Setsompop, K., Feinberg, D.A., Polimeni, J.R., 2016. Rapid brain MRI acquisition techniques at ultra-high fields. *NMR Biomed.* 29, 1198–1221. <https://doi.org/10.1002/nbm.3478>.
- Setsompop, K., Fan, Q., Stockmann, J., Bilgic, B., Huang, S., Cauley, S.F., Nummenmaa, A., Wang, F., Rathi, Y., Witzel, T., Wald, L.L., 2018. High-resolution in vivo diffusion imaging of the human brain with generalized slice dithered enhanced resolution: simultaneous multislice (gSlider-SMS). *Magn. Reson. Med.* 79, 141–151. <https://doi.org/10.1002/mrm.26653>.
- Shafee, R., Buckner, R.L., Fischl, B., 2015. Gray matter myelination of 1555 human brains using partial volume corrected MRI images. *NeuroImage* 105, 473–485. <https://doi.org/10.1016/j.neuroimage.2014.10.054>.
- Shemesh, N., Álvarez, G.A., Frydman, L., 2015. Size distribution imaging by non-uniform oscillating-gradient spin echo (NOGSE) MRI. *PLoS One* 10. <https://doi.org/10.1371/journal.pone.0133201> e0133201.
- Shemesh, N., Jespersen, S.N., Alexander, D.C., Cohen, Y., Drobnyak, I., Dyrby, T.B., Finsterbusch, J., Koch, M.A., Kuder, T., Laun, F., Lawrenz, M., Lundell, H., Mitra, P.P., Nilsson, M., Özarslan, E., Topgaard, D., Westin, C.F., 2016. Conventions and nomenclature for double diffusion encoding NMR and MRI. *Magn. Reson. Med.* 75, 82–87. <https://doi.org/10.1002/mrm.25901>.
- Shepherd, T.M., Flint, J.J., Thelwall, P.E., Stanisz, G.J., Mareci, T.H., Yachnis, A.T., Blackband, S.J., 2009. Postmortem interval alters the water relaxation and diffusion properties of rat nervous tissue – implications for MRI studies of human autopsy samples. *NeuroImage* 44, 820–826. <https://doi.org/10.1016/j.neuroimage.2008.09.054>.
- Sled, J.G., 2018. Modelling and interpretation of magnetization transfer imaging in the brain. *NeuroImage* 182, 128–135.
- Stanisz, G.J., Kecojovic, A., Bronskill, M.J., Henkelman, R.M., 1999. Characterizing white matter with magnetization transfer and T_2 . *Magn. Reson. Med.* 42, 1128–1136. [https://doi.org/10.1002/\(SICI\)1522-2594\(199912\)42:6<1128::AID-MRM18>3.0.CO;2-9](https://doi.org/10.1002/(SICI)1522-2594(199912)42:6<1128::AID-MRM18>3.0.CO;2-9).
- Stikov, N., Pike, G.B., this special issue. Microstructural imaging of white matter. *NeuroImage* (in press).
- Stikov, N., Boudreau, M., Levesque, I.R., Tardif, C.L., Barral, J.K., Pike, G.B., 2015. On the accuracy of T_1 mapping: searching for common ground. *Magn. Reson. Med.* 73, 514–522. <https://doi.org/10.1002/mrm.25135>.
- Stüber, C., Morawski, M., Schäfer, A., Labadie, C., Wähnert, M., Leuze, C., Streicher, M., Barapatre, N., Reimann, K., Geyer, S., Spemann, D., Turner, R., 2014. Myelin and iron concentration in the human brain: a quantitative study of MRI contrast. *NeuroImage* 93, 95–106. <https://doi.org/10.1016/j.neuroimage.2014.02.026>.
- Stucht, D., Danishad, K.A., Schulze, P., Godenschweiger, F., Zaitsev, M., Speck, O., 2015. Highest resolution in vivo human brain MRI using prospective motion correction. *PLoS One* 10, e0133921. <https://doi.org/10.1371/journal.pone.0133921>.
- Sundgren, P.C., Dong, Q., Gómez-Hassan, D., Mukherji, S.K., Maly, P., Welsh, R., 2004. Diffusion tensor imaging of the brain: review of clinical applications. *Neuroradiology* 46, 339–350. <https://doi.org/10.1007/s00234-003-1114-x>.
- Symms, M., Jäger, H.R., Schmierer, K., Yousry, T.A., 2004. A review of structural magnetic resonance neuroimaging. *J. Neurol. Neurosurg. Psychiatry* 75, 1235–1244. <https://doi.org/10.1136/jnnp.2003.032714>.
- Tabelow, K., Mohammadi, S., Weiskopf, N., Polzehl, J., 2015. POAS4SPM: a toolbox for SPM to denoise diffusion MRI data. *Neuroinformatics* 13, 19–29. <https://doi.org/10.1007/s12021-014-9228-3>.
- Tardif, C.L., Schäfer, A., Waehnert, M., Dinse, J., Turner, R., Bazin, P.L., 2015. Multi-contrast multi-scale surface registration for improved alignment of cortical areas. *NeuroImage* 111, 107–122. <https://doi.org/10.1016/j.neuroimage.2015.02.005>.
- Todorich, B., Pasquini, J.M., Garcia, C.I., Paez, P.M., Connor, J.R., 2009. Oligodendrocytes and myelination: the role of iron. *Glia* 57, 467–478. <https://doi.org/10.1002/glia.20784>.
- Tofts, P. (Ed.), 2004a. Quantitative MRI of the Brain. John Wiley & Sons, Ltd.
- Tofts, P.S., 2004b. PD: proton density of tissue water. in: *Tofts (2004a)*. chapter 8, pp. 83–109. <https://doi.org/10.1002/0470869526.ch4>.
- Tofts, P.S., Steens, S.C.A., van Buchem, M.A., 2004. MT: magnetization transfer. in: *Tofts (2004a)*. chapter 8, pp. 257–298. <https://doi.org/10.1002/0470869526.ch8>.
- Tomassy, G.S., Berger, D.R., Chen, H.H., Kasthuri, N., Hayworth, K.J., Vercelli, A., Seung, H.S., Lichtman, J.W., Arlotta, P., 2014. Distinct profiles of myelin distribution along single axons of pyramidal neurons in the neocortex. *Science* 344, 319–324. <https://doi.org/10.1126/science.1249766>.
- Trampel, R., Ott, D.V.M., Turner, R., 2011. Do the congenitally blind have a stria of Gennari? First intracortical insights in vivo. *Cereb. Cortex* 21, 2075–2081. <https://doi.org/10.1093/cercor/bhq282>.
- Trampel, R., Bazin, P.L., Pine, K., Weiskopf, N., 2018. In-vivo magnetic resonance imaging (MRI) of laminae in the human cortex. *NeuroImage*. <https://doi.org/10.1016/j.neuroimage.2017.09.037> (in press).
- Turner, R., De Haan, D., 2017. Bridging the gap between system and cell: the role of ultra-high field MRI in human neuroscience. In: Mahfoud, T., McLean, S., Rose, N. (Eds.), *Vital Models: The Making and Use of Models in the Brain Sciences*. Volume 233 of *Progress in Brain Research*, chapter 8, pp. 179–220. <https://doi.org/10.1016/bs.pbr.2017.05.005>.
- Ulrich, X., Yablonskiy, D.A., 2016. Separation of cellular and BOLD contributions to T_2^* signal relaxation. *Magn. Reson. Med.* 75, 606–615. <https://doi.org/10.1002/mrm.25610>.
- Ułudağ, K., Dubowitz, D.J., Buxton, R.B., 2005. Basic principles of functional MRI. In: *Clinical Magnetic Resonance Imaging*, pp. 249–287.
- van Duijn, S., Bulk, M., Duinen, V.G.S., Nabuurs, R.J.A., Buchem, V.A.M., van der Weerd, L., Natté, R., 2017. Cortical iron reflects severity of Alzheimer's disease. *J. Alzheimer's Dis.* 60, 1533–1545. <https://doi.org/10.3233/JAD-161143>.
- Van Essen, D.C., Ugurbil, K., Auerbach, E., Barch, D., Behrens, T.E.J., Bucholz, R., Chang, A., Chen, L., Corbetta, M., Curtiss, S.W., Della Penna, S., Feinberg, D., Glasser, M.F., Harel, N., Heath, A.C., Larson-Prior, L., Marcus, D., Michalareas, G., Moeller, S., Oostenveld, R., Petersen, S.E., Prior, F., Schlaggar, B.L., Smith, S.M., Snyder, A.Z., Xu, J., Yacoub, E., 2012. The Human Connectome Project: a data acquisition perspective. *NeuroImage* 62, 2222–2231. <https://doi.org/10.1016/j.neuroimage.2012.02.018>.
- Van Nguyen, D., Grebenkov, D., Le Bihan, D., Li, J.R., 2015. Numerical study of a cylinder model of the diffusion MRI signal for neuronal dendrite trees. *J. Magn. Reson.* 252, 103–113. <https://doi.org/10.1016/j.jmr.2015.01.008>.
- van Zijl, P.C.M., Yadav, N.N., 2011. Chemical exchange saturation transfer (CEST): what is in a name and what isn't? *Magn. Reson. Med.* 65, 927–948. <https://doi.org/10.1002/mrm.22761>.
- Vavasour, I.M., Laule, C., Li, D.K., Traboulsee, A.L., MacKay, A.L., 2011. Is the magnetization transfer ratio a marker for myelin in multiple sclerosis? *J. Magn. Reson. Imag.* 33, 710–718. <https://doi.org/10.1002/jmri.22441>.
- Veraart, J., Novikov, D.S., Christiaens, D., Aides-Aron, B., Sijbers, J., Fieremans, E., 2016. Denoising of diffusion MRI using random matrix theory. *NeuroImage* 142, 394–406. <https://doi.org/10.1016/j.neuroimage.2016.08.016>.
- Versluis, M.J., Peeters, J.M., van Rooden, S., van der Grond, J., van Buchem, M.A., Webb, A.G., van Osch, M.J.P., 2010. Origin and reduction of motion and f_0 artifacts in high resolution T_2^* -weighted magnetic resonance imaging: application in Alzheimer's disease patients. *NeuroImage* 51, 1082–1088. <https://doi.org/10.1016/j.neuroimage.2010.03.048>.
- Vinogradov, E., Sherry, A.D., Lenkinski, R.E., 2013. CEST: from basic principles to applications, challenges and opportunities. *J. Magn. Reson.* 229, 155–172. <https://doi.org/10.1016/j.jmr.2012.11.024>.
- Vogt, C., Vogt, O., 1919. *Allgemeine Ergebnisse unserer Hirnforschung*. J. Psychol. Neurol. 25, 275–462.
- von Economo, C.F., Koskinas, G.N., 1925. *Die Cytoarchitektonik der Hirnrinde des erwachsenen Menschen*. J. Springer.
- Waehnert, M.D., Dinse, J., Schäfer, A., Geyer, S., Bazin, P.L., Turner, R., Tardif, C.L., 2016. A subject-specific framework for in vivo myeloarchitectonic analysis using high resolution quantitative MRI. *NeuroImage* 125, 94–107. <https://doi.org/10.1016/j.neuroimage.2015.10.001>.
- Wallace, M.N., Cronin, M.J., Bowtell, R.W., Scott, I.S., Palmer, A.R., Gowland, P.A., 2016. Histological basis of laminar MRI patterns in high resolution images of fixed human auditory cortex. *Front. Neurosci.* 10, 455. <https://doi.org/10.3389/fnins.2016.00455>.
- Warnking, J., Dojat, M., Guérin-Dugué, A., Delon-Martin, C., Olympeff, S., Richard, N., Chéhikian, A., Segebarth, C., 2002. fMRI retinotopic mapping—step by step. *NeuroImage* 17, 1665–1683. <https://doi.org/10.1006/nimg.2002.1304>.
- Wasserthal, C., Brechmann, A., Stadler, J., Fischl, B., Engel, K., 2014. Localizing the human primary auditory cortex in vivo using structural MRI. *NeuroImage* 93, 237–251. <https://doi.org/10.1016/j.neuroimage.2013.07.046>.
- Wei, H., Xie, L., Bibb, R., Li, W., Decker, K., Zhang, Y., Johnson, G.A., Liu, C., 2016. Imaging whole-brain cytoarchitecture of mouse with MRI-based quantitative susceptibility mapping. *NeuroImage* 137, 107–115. <https://doi.org/10.1016/j.neuroimage.2016.05.033>.
- Weiskopf, N., Suckling, J., Williams, G., Correia, M.M., Inkster, B., Tait, R., Ooi, C., Bullmore, E.T., Lutti, A., 2013. Quantitative multi-parameter mapping of R_1 , PD^* , MT , and R_2^* at 3T: a multi-center validation. *Front. Neurosci.* 7, 95. <https://doi.org/10.3389/fnins.2013.00095>.
- Weiskopf, N., Mohammadi, S., Lutti, A., Callaghan, M.F., 2015. Advances in MRI-based computational neuroanatomy: from morphometry to in-vivo histology. *Curr. Opin. Neurol.* 28, 313–322. <https://doi.org/10.1097/WCO.0000000000000222>.
- West, K.L., Kelm, N.D., Carson, R.P., Gochberg, D.F., Ess, K.C., Does, M.D., 2018. Myelin volume fraction imaging with MRI. *NeuroImage* 182, 511–521.
- Wharton, S., Bowtell, R., 2012. Fiber orientation-dependent white matter contrast in gradient echo MRI. *Proc. Natl. Acad. Sci.* 109, 18559–18564. <https://doi.org/10.1073/pnas.1211075109>.
- Whitaker, K.J., Vértés, P.E., Romero-García, R., Váša, F., Moutoussis, M., Prabhu, G., Weiskopf, N., Callaghan, M.F., Wagstyl, K., Rittman, T., Tait, R., Ooi, C., Suckling, J., Inkster, B., Fonagy, P., Dolan, R.J., Jones, P.B., Goodyer, I.M., the NSNP Consortium, Bullmore, E.T., 2016. Adolescence is associated with genomically patterned consolidation of the hubs of the human brain connectome. *Proc. Natl. Acad. Sci.* 113, 9105–9110. <https://doi.org/10.1073/pnas.1601745113>.
- Wilm, B.J., Nagy, Z., Barmet, C., Vannesjo, S.J., Kasper, L., Haeblerlin, M., Gross, S., Dietrich, B.E., Brunner, D.O., Schmid, T., Pruessmann, K.P., 2015. Diffusion MRI with concurrent magnetic field monitoring. *Magn. Reson. Med.* 74, 925–933. <https://doi.org/10.1002/mrm.25827>.

- Xu, T., Foxley, S., Kleinnijenhuis, M., Chen, W.C., Miller, K.L., 2018. The effect of realistic geometries on the susceptibility-weighted MR signal in white matter. *Magn. Reson. Med.* 79, 489–500. <https://doi.org/10.1002/mrm.26689>.
- Yablonskiy, D.A., Haacke, E.M., 1994. Theory of NMR signal behavior in magnetically inhomogeneous tissues: the static dephasing regime. *Magn. Reson. Med.* 32, 749–763. <https://doi.org/10.1002/mrm.1910320610>.
- Yablonskiy, D.A., Sukstanskii, A.L., 2017. Effects of biological tissue structural anisotropy and anisotropy of magnetic susceptibility on the gradient echo MRI signal phase: theoretical background. *NMR Biomed.* 30, e3655 <https://doi.org/10.1002/nbm.3655>.
- Yacoub, E., Harel, N., Ugurbil, K., 2008. High-field fMRI unveils orientation columns in humans. *Proc. Natl. Acad. Sci.* 105, 10607–10612. <https://doi.org/10.1073/pnas.0804110105>.
- Yang, D.M., Huettner, J.E., Bretthorst, G.L., Neil, J.J., Garbow, J.R., Ackerman, J.J., 2018. Intracellular water preexchange lifetime in neurons and astrocytes. *Magn. Reson. Med.* 79, 1616–1627. <https://doi.org/10.1002/mrm.26781>.
- Yao, B., Li, T.Q., van Gelderen, P., Shmueli, K., de Zwart, J.A., Duyn, J.H., 2009. Susceptibility contrast in high field MRI of human brain as a function of tissue iron content. *NeuroImage* 44, 1259–1266. <https://doi.org/10.1016/j.neuroimage.2008.10.029>. Corrigendum: Yao et al. (2012).
- Yao, B., Li, T.Q., van Gelderen, P., Shmueli, K., de Zwart, J.A., Duyn, J.H., 2012. Corrigendum to “Susceptibility contrast in high field MRI of human brain as a function of tissue iron content” [*NeuroImage* 44/4 (2009) 1259–1266]. *NeuroImage* 62, 2173. <https://doi.org/10.1016/j.neuroimage.2012.03.055>.
- Ye, L., Allen, W.E., Thompson, K.R., Tian, Q., Hsueh, B., Ramakrishnan, C., Wang, A.C., Jennings, J.H., Adhikari, A., Halpern, C.H., Witten, I.B., Barth, A.L., Luo, L., McNab, J.A., Deisseroth, K., 2016. Wiring and molecular features of prefrontal ensembles representing distinct experiences. *Cell* 165, 1776–1788. <https://doi.org/10.1016/j.cell.2016.05.010>.
- Zatorre, R.J., Fields, R.D., Johansen-Berg, H., 2012. Plasticity in gray and white: neuroimaging changes in brain structure during learning. *Nat. Neurosci.* 15, 528–536. <https://doi.org/10.1038/nn.3045>.
- Zecca, L., Youdim, M.B.H., Riederer, P., Connor, J.R., Crichton, R.R., 2004. Iron, brain ageing and neurodegenerative disorders. *Nat. Rev. Neurosci.* 5, 863–873. <https://doi.org/10.1038/nrn1537>.
- Zeki, S., 1993. *A Vision of the Brain*. Blackwell Scientific Publications, Oxford. First published 1993. Reprinted with corrections 1994.
- Zhang, H., Schneider, T., Wheeler-Kingshott, C.A., Alexander, D.C., 2012. NODDI: practical in vivo neurite orientation dispersion and density imaging of the human brain. *NeuroImage* 61, 1000–1016. <https://doi.org/10.1016/j.neuroimage.2012.03.072>.
- Zhang, J., Kolind, S.H., Laule, C., MacKay, A.L., 2015. Comparison of myelin water fraction from multiecho T₂ decay curve and steady-state methods. *Magn. Reson. Med.* 73, 223–232. <https://doi.org/10.1002/mrm.25125>.
- Zhao, Y., Wen, J., Cross, A.H., Yablonskiy, D.A., 2016. On the relationship between cellular and hemodynamic properties of the human brain cortex throughout adult lifespan. *NeuroImage* 133, 417–429. <https://doi.org/10.1016/j.neuroimage.2016.03.022>.
- Zhao, Y., Raichle, M.E., Wen, J., Benzinger, T.L., Fagan, A.M., Hassenstab, J., Vlassenko, A.G., Luo, J., Cairns, N.J., Christensen, J.J., Morris, J.C., Yablonskiy, D.A., 2017. In vivo detection of microstructural correlates of brain pathology in preclinical and early Alzheimer disease with magnetic resonance imaging. *NeuroImage* 148, 296–304. <https://doi.org/10.1016/j.neuroimage.2016.12.026>.
- Zilles, K., Amunts, K., 2010. Centenary of Brodmann's map – conception and fate. *Nat. Rev. Neurosci.* 11, 139–145. <https://doi.org/10.1038/nrn2776>.
- Zilles, K., Schleicher, A., Palomero-Gallagher, N., Amunts, K., 2002. Quantitative analysis of cyto- and receptor architecture of the human brain. In: Toga, A., Mazziotta, J. (Eds.), *Brain Mapping: the Methods*, second ed. Academic Press, San Diego, pp. 573–602. <https://doi.org/10.1016/B978-012693019-1/50023-X>.
- Zilles, K., Bacha-Trams, M., Palomero-Gallagher, N., Amunts, K., Friederici, A.D., 2015. Common molecular basis of the sentence comprehension network revealed by neurotransmitter receptor fingerprints. *Cortex* 63, 79–89. <https://doi.org/10.1016/j.cortex.2014.07.007>.